AgriCarbon-EO v1.0.1: Large Scale and High-Resolution Simulation of Carbon Fluxes by Assimilation of Sentinel-2 and Landsat-8 Reflectances using a Bayesian approach

Taeken Wijmer[1,2,*], Ahmad Al Bitar[1,*], Ludovic Arnaud[1], Remy Fieuzal[1], and Eric Ceschia[1]
[1]CESBIO, Université de Toulouse, CNES/CNRS/INRAE/IRD/UPS, 18 Avenue Edouard Belin, bpi 2801, CEDEX 09, 31401 Toulouse, France
[2]DYNAFOR, Université de Toulouse, INRAE, INPT, INP-PURPAN, Castanet-Tolosan, France
Correspondence: Taeken Wijmer (taeken.wijmer@cesbio.cnes) and Ahmad Al Bitar (ahmad.albitar@gmx.com)

Abstract. Soil organic carbon storage is a well-identified climate change mitigation solution. An extensive quantification of the soil carbon storage in cropland for agricultural policy and offset carbon markets using in-situ measurements would be excessively costly, especially at the intrafield scale. For this reason, comprehensive monitoring, reporting, and verification (MRV) of soil carbon and its explanatory variables at a large scale need to rely on remote sensing and modelling tools that provide the spatiotemporal dynamics of the carbon budget components with the associated uncertainties at high resolution. In this paper, we present AgriCarbon-EO v1.0.1: an end-to-end processing chain that enables the estimation of carbon budget components of major crops and cover crops at intrafield resolution (10 m) and large scale (over 110×110 km) by assimilating remote sensing data in physically-based radiative transfer and agronomic models. The data assimilation in AgriCarbon-EO is based on a novel Bayesian approach that combines normalized importance sampling (NIS) and look-up table (LUT) generation. This approach propagates the uncertainties across the processing chain from the reflectances to the output variables. The chain inputs are land cover maps, multispectral reflectance maps from the Sentinel-2 and Landsat-8 satellites, and daily weather forcing. In the first step, inverse modelling of the PROSAIL radiative transfer model was performed to obtain the green leaf area index ($GLAI$). The $GLAI$ time series are then assimilated into the SAFYE-CO2 crop model while taking into consideration their uncertainties. After a presentation, the chain is applied over winter wheat in the southwest of France during the cropping seasons from 2017 to 2019. We compare the results against the net ecosystem exchange measured at the FR-AUR ICOS flux site (RMSE = 1.68 - 2.38 $\mathrm{gC\,m^{-2}}$, R^2 = 0.87 - 0.77), biomass (RMSE = 11.34 $\mathrm{g\,m^{-2}}$, R^2 = 0.94), and yield maps obtained from combine harvesters. We also quantified the difference between pixel and field scale simulations of biomass (bias = -47 $\mathrm{g\,m^{-2}}$, -39 % variability), and the impact of the number of remote sensing acquisitions on the outputs (-66 % of mean uncertainty of biomass).

Keywords: MRV; Carbon Farming; crop modelling; Sentinel-2; Normalized Importance Sampling

1 Introduction

Agriculture and land use changes account for 15% *i.e.* (8.7 Gt CO_2 yr^{-1}) of human-induced greenhouse gas (GHG) emissions (Pörtner et al., 2022; Skea et al., 2022). Agriculture has also been identified as a sector that can contribute to climate mitigation through several solutions (Porter et al., 2017; Matthews et al., 2022). Among these, soil organic carbon (SOC) storage has the potential to remove 0.6 to 9.3 Gt CO_2 yr^{-1}) from the atmosphere through the implementation of carbon farming practices (Skea et al., 2022). Increasing the SOC implies an enhancement of the net ecosystem carbon budget (NECB) (Woodwell and Whittaker (1968),Chapin et al. (2006),Smith et al. (2010))expressed in Equation 1. A positive variation of NECB can be achieved by increasing the gross primary production (GPP) and the net ecosystem exchange (NEE) through aboveground crop residue retention (Soussana et al. (2019),Bolinder et al. (2020)), the addition of cover crops in crop rotations (Poeplau and Don, 2015; Lugato et al., 2020), and an increase of the carbon imports through the application of organic amendments (Bolinder et al., 2020) and biochar (Steinbeiss et al., 2009).

$$NECB = \overbrace{\overbrace{GPP \rlap{$\underbrace{}_{Reco}$} - Rauto}^{NPP} - Rh}^{NEE} + C_{imports} - C_{exports} \tag{1}$$

Equation 1 also shows the importance of 1) the quantification of the effect of ecosystem respiration ($Reco$) which is subdivided into autotrophic (plant) and heterotrophic (soil) respiration ($Rauto$ and Rh), and 2) the quantification of carbon exports that mainly correspond to yield and the fraction of biomass incorporated to the soil.

It should be noted that after the death of the vegetation, all the unharvested biomass returns to the soil. At this point, we can approximate that $NECB = \Delta SOC$. The accumulation of SOC in agricultural soils, in addition to climate change mitigation, has additional benefits in terms of ecosystem soil services (ESS), such as increasing soil fertility (Su et al., 2006), enhancing water holding capacity (Karhu et al., 2011) and increasing biodiversity (Wall et al., 2015). SOC storage could also provide an additional source of revenue for farmers through carbon credits and subsidies.

Following the Intergovernmental Panel on Climate Change guidelines for national GHG inventories, methodologies for assessing SOC stock changes have been developed. They are based on a tiered approach with increasing complexity involving soil monitoring networks where SOC is directly measured and process-based modelling where Δ SOC is modelled by taking into account the soil, climate, and mean biomass returned to the soil (GPP-$Rauto$-$Cexport$) derived from yield at theregional scale (e.g. Yasso07 in Finland, RothC in Japan, DayCent in the USA). The need to monitor soil carbon at the farm and field levels to inform individual farmers, and guide policies and the development of carbon markets has led to the development of monitoring reporting and verification (MRV) schemes based on similar approaches employed at a higher resolution (Smith et al., 2020; Paustian et al., 2019). These approaches are mainly used in carbon farming projects following national or regional initiatives (e.g. Label Bas Carbone in France). They often rely on a soil-centred quantification approach where the focus is the modelling of Rh, $Cimports$, and $Cexports$. In these approaches, the estimates of carbon returned to the soil are usually extrapolated from farm- or field-scale yield information (Clivot et al., 2019). The field-scale often does not match the intrafield/farm variability of the soil characteristics and plant growth (de Gruijter et al., 2016; Ellili et al., 2019). This means that these values present limitations in terms of accuracy and spatial representativity.

Coupled plant/soil process-based models that address the quality and quantity of the crop residues that return to the soil are also used to assess SOC stock changes. These models include the main components of the cropland's biological $\mathrm{CO_2}$ fluxes. They can also account for carbon inputs through organic fertilization and carbon exports of biomass at harvest (Equation 1, (Smith et al., 2010). Existing agronomic models such as, DSSAT-CSM (Porter et al., 2010), STICS (Launay et al., 2021), DAYCENT (Parton et al., 1998) and WOFOST (Supit et al., 1994), soil models, e.g. DNDC (Gilhespy et al., 2014), and land surface models, e.g. ORCHIDEE-STICS (Gervois et al., 2008), take into account a wide array of environmental conditions to represent crop growth and the components of the carbon budget (Equation 1). However, water and nutrient availability, local topography, pests, and historical factors (e.g. former ditches, roads, field limits) highly influence soil and plant processes (Gregory et al., 2009). This can result in high spatiotemporal variability in crop development and soil processes that can be observed even at the intrafield scale (Stevens et al., 2008; de Gruijter et al., 2016). Moreover, to operate those models, farmer activity data and crop development dynamics are required to provide accurate estimates of SOC stock changes. Getting hold of this information at a large scale is still challenging (Seidel et al., 2018; Wattenbach et al., 2010). However, it is possible to use time series of biophysical variables such as $GLAI$, derived from remote sensing data, to provide information about development dynamics to those models through data assimilation (Huang et al., 2019; Battude et al., 2017; Pique et al., 2020a). These assimilated observations provide spatially explicit crop-specific estimates of biomass and carbon returned to the soil using coupled soil-plant models. Assimilation of biophysical variables is usually based on iterative optimization methods such as Simplex, Monte-Carlo Markov Chain (MCMC), ensemble Kalman filter, or variational assimilation that are generally applied at moderate resolutions (Kumar et al., 2019; Hararuk et al., 2014) or field scale (Trepos et al., 2020; Upreti et al., 2020). Applying those methods at an intrafield resolution over large areas is often computationally prohibitive. Enhancing scalability is thus key to assessing the spatial variability of $\mathrm{CO_2}$ flux components at a scale consistent with measurements of soil and plant characteristics. Operating on a scale that is representative of measurements enables better diagnosis and calibration of plant and soil processes, as well as a more robust validation and uncertainty estimation of the model outputs.

The aim of this paper is to present the newly developed AgriCarbon-EO processing chain for the assimilation of Earth Observation (EO) data into the SAFYE-CO2 agronomic model at large scale ($100\ \mathrm{km}$) and intrafield resolution ($10\ \mathrm{m}$). This processing chain allows for the assessment of the carbon budget components (Equation 1). The challenge of estimating the carbon budget components at high spatial resolution at a large scale is addressed by using the new BASALT (BAyesian normalized importance SAmpling via Look-up Table generation) algorithm, which also provides uncertainty estimates. In addition, the paper aims to provide an evaluation of the accuracy, limitations, and robustness of AgriCarbon-EO methods through validation exercises and scenario simulations. We chose to make these assessments for wheat in Southwest France, as this area benefits from a large amount of data that has been gathered in the context of the Observatoire Spatial Regional (OSR), and the Integrated Carbon Observation System (ICOS) network. Furthermore, Southwest France is a major production area of wheat. This area has also been chosen because it presents a challenge for spatial crop modelling in reproducing the diverse crop growth dynamics induced by a wide array of pedo-climatic conditions in a hilly landscape. The scenario simulations were designed to assess the robustness of the method with respect to the amount of assimilated remote sensing data, and the added value in using high-resolution agronomic modelling.

In the following sections, we first present the details of the AgriCarbon-EO processing chain including the standard inputs, models, and BASALT assimilation scheme. We then present the numerical experimental setup and the validation datasets. Next, we present the validation results and the impact of image availability. Finally, we conclude with the benefits and limitations of the presented solution for assessing the cropland carbon budget components and their associated uncertainties at high resolution over large areas.

2 AgriCarbon-EO chain

2.1 Overview of the processing chain

AgriCarbon-EO is an end-to-end processing chain that simulates multiple relevant variables of crop development, biomass inputs to the soil, CO_2 fluxes, and water at a daily timescale, for the assessment of carbon and water budgets. It is specifically designed to assimilate optical remote sensing datasets at native high resolution into a simple but generic agronomic model (SAFYE-CO2) over large territories. A brief description of the data flow and processing steps is presented here (Figure 1) and detailed in the following subsections:

1. A preprocessing "Data ingestion" step allows the updating of existing datasets through automated downloading of satellite images and weather forcing. Optical bottom of atmosphere (BOA) reflectances are downloaded for Sentinel-2 and Landsat-8 (referred to as S2 and L8 below). Satellite data are uncompressed and relevant spectral bands are stacked. The weather data are stored in time series with the associated correspondence matrix to the high-resolution grid defined by the user. This is performed for the zone defined by the input land cover (polygons or mask raster map).
2. The biophysical variable $GLAI$ is retrieved from the satellite reflectance images by inverting a radiative transfer model (PROSAIL). The retrieval of $GLAI$ is based on an adapted Bayesian importance sampling procedure (*i.e.* BASALT). In this step, a spatial application of the retrieval model is done for each satellite image.
3. The crop model (SAFYE-CO2) parameters are inverted by assimilating the $GLAI$ time series using the BASALT method as in the previous step. In this case, LUTs are generated based on the closest known weather simulation node. Only the phenological crop model parameters and the light use efficiency (LUE) are inverted in this procedure.
4. A postprocessing step allows the construction of the output products based on the posterior crop model parameter distribution. Georeferenced maps of the variables of interest in each model (*i.e.* PROSAIL, SAFYE-CO2) are constructed as well as cumulative variables (e.g. NEP which is the cumulative NEE over one cropping year, number of satellite acquisitions, and soil water content).

120 AgriCarbon-EO is implemented in the Python language. A maximum requirement of 5 GB per process for the satellite images needs to be considered. This will allow mono-process tests and development on standard computers over smaller study areas, as well as large-scale applications (e.g. 100×100 km) with high-performance computing (HPC) resources.

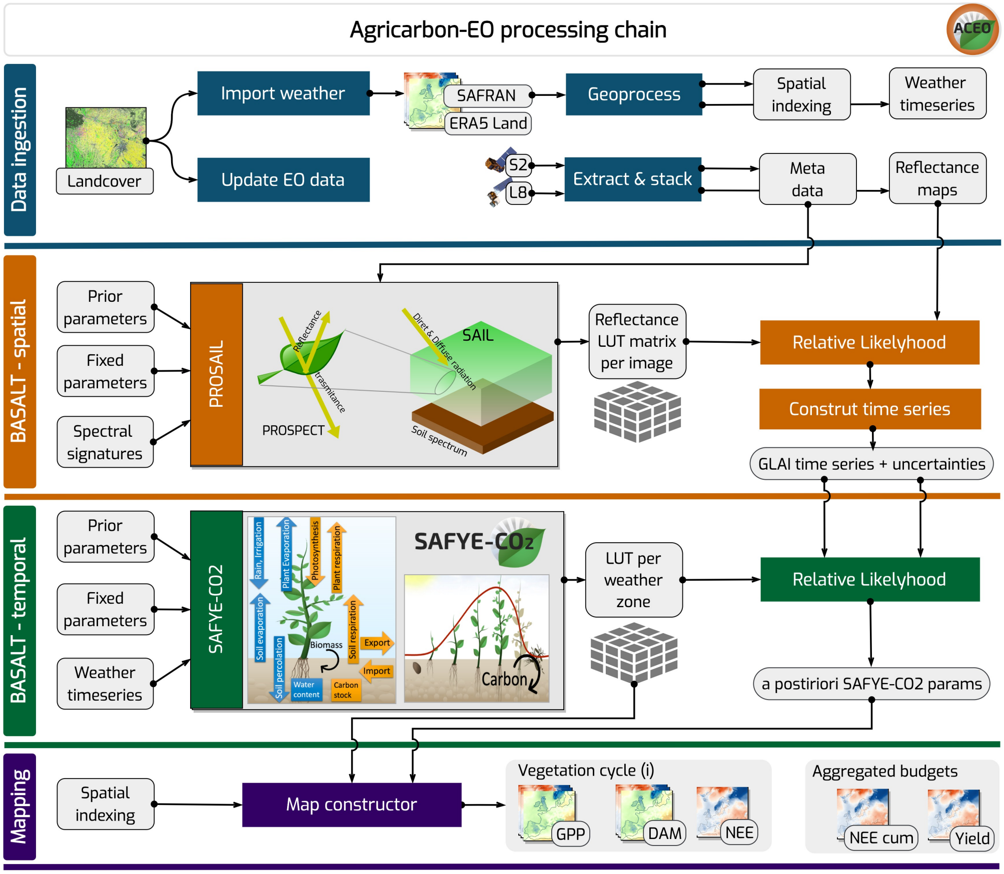

Figure 1. Overview of the AgriCarbon-EO data flow and main processing steps that include the data ingestion, BASALT spatial retrieval, BASALT temporal retrieval, and mapping of the variables of interest.

2.2 Input dataset

In the following subsections, the spatial datasets needed for AgriCarbon-EO are detailed with the corresponding sources.

125 2.2.1 Land cover map

The main driver for the data preparation is a land cover (LC) map in vector format (shapefile). This file should contain the boundaries of each agricultural field for a given cropping year over a selected region of interest (*i.e.* border extents of the LC shapefile). Based on the border extents of the LC map, the remote sensing and weather forcing data are downloaded and preprocessed. When the simulations are intended to cover several cash crop cycles a run scenario of AgriCarbon-EO is considered for each individual crop cycle. Additionally, a standard simulation can include a cover crop with each cash crop. In this paper, AgriCarbon-EO was applied to winter wheat crops in Southwest France (on the Sentinel-2 tile referenced as 31TCJ) in 2017, 2018, and 2019. The LC map was obtained from the Registre Parcellaire Graphique (RPG) in France ("RPG," 2021), which is available online in open licence v2.0. This information is produced by the Institut Geographique National (IGN) for the Agence de Service de Paiement (ASP *i.e.* The French Paying Agency) in charge of the implementation, control, and payment of the subsidies for the EU Common Agricultural Policy (CAP) in France. In this study, the original polygons in the Lambert-93 projection (EPSG:2154 - RGF93) were reprojected to a selected common grid projection, WGS 84/UTM31.

2.2.2 BOA surface reflectances

The assimilated remote sensing data are optical surface reflectances at the BOA, which correspond to reflected energy from the top of the canopy and the soil at a given incidence angle, for a set of observed spectral bands. Currently, AgriCarbon-EO uses data from the ESA's Sentinel-2 program (Drusch et al., 2012) and NASA's Landsat-8 program (Roy et al., 2014), knowing that the modular interface is compatible with multisource EO data. The Sentinel-2 data are acquired over 13 optical bands with a resolution of 10 to 60 m depending on the spectral bands with a 5-day revisit from the constellation. Only the nine visible bands were considered from the Landsat-8 data. Landsat-8 has a revisit of 16 days and a spatial resolution of 30 m in the visible range.

For this study, the data were downloaded from the Thematic Center for Continental Surfaces (THEIA), which uses a common atmospheric correction and cloud masking algorithm for Sentinel-2 and Landsat-8 through the MAJA processing chain (Hagolle et al., 2021). This enables a harmonized Level-2A database with an efficient cloud masking algorithm (Baetens et al., 2019). The data contain quality indicators, including cloud coverage. The datasets are presented as granules (tiles) of 110×110 km orthoimages in the UTM projection. Prior to the processing, the remote sensing datasets are decompressed and resampled at 10 m resolution using nearest-neighbour.

2.2.3 Weather forcing data

Daily weather data maps covering the simulation period and spatial extents are used to force the crop model. Cumulative daily global incoming solar radiation (Rg in $\mathrm{MJ\,m^{-2}}$) and daily average air temperature at 2 m (Ta in °C) are needed for the vegetation growth module in SAFYE-CO2. Based on previous studies that showed the impact of diffuse radiation on crop development and photosynthesis (Béziat, 2009; Roderick et al., 2001), the diffuse incoming radiation is computed based on De Jong (1980). Furthermore, two additional datasets are needed for the water budget module of SAFYE-CO2: daily potential evapotranspiration ($ET0$ in $\mathrm{mm\,d^{-1}}$) and daily cumulative rainfall ($Rain$ in $\mathrm{mm\,d^{-1}}$). AgriCarbon-EO supports two data sources that provide weather data: the Météo-France SAFRAN dataset (Vidal et al., 2010) and ERA5 Land (Muñoz-Sabater et al., 2021). The extraction of the ERA5 Land data was performed via the dedicated API. SAFRAN consists of a reanalysis of climate variables at 8 km spatial resolution and the hourly timescale over France starting 1958. In this paper, the weather data were extracted from the Météo-France SAFRAN dataset and reprojected over the UTM/31N at 8 km resolution.

2.3 Process-based models

2.3.1 Radiative transfer modelling using PROSAIL

Maps of geophysical variables (*i.e.* $GLAI$) are retrieved in AgriCarbon-EO by inverting the PROSAIL radiative transfer model. PROSAIL has been extensively used as a radiative transfer model for vegetated areas (Jacquemoud et al., 2009) with a wide range of inversion schemes (Wang et al., 2022). PROSAIL combines the PROSPECT and SAIL models (Baret et al., 1992). PROSPECT provides leaf spectral properties in the 400 nm to 2500 nm wavelength (Jacquemoud and Baret, 1990). SAIL (scattering by arbitrary inclined leaves) is a multidirectional canopy reflectance model (Verhoef, 1984) based on the bidirectional reflectance model (Suits, 1971). A Python implementation of PROSAIL was used in AgriCarbon-EO. This version includes the coupled PROSAIL from PROSPECT-5-D (Féret et al., 2017), 4SAIL (Verhoef et al., 2007), and a simple Lambertian soil reflectance model. The PROSAIL parameters were inverted using a Bayesian approach in order to provide $GLAI$ and its corresponding uncertainty as input to the crop model inversion.

2.3.2 Crop CO2 fluxes and biomass modelling using SAFYE-CO2

SAFYE-CO2 is a parsimonious agronomic model that runs at a daily time-step (Veloso, 2014; Pique et al., 2020a, b). The model stems from the SAFY models (Duchemin et al., 2008; Battude et al., 2017) which compute DAM, based on the LUE theory of Monteith et al. (1977). A full description of the SAFYE-CO2 model is provided in Veloso (2014); Pique et al. (2020a, b). The core equations of the model are detailed below. In SAFYE-CO2, NEE is computed based on Rh and NPP ($\mathrm{gC\,m^{-2}}$), which in turn is computed from GPP ($\mathrm{gC\,m^{-2}}$) by subtracting autotrophic respiration $Rauto$ ($\mathrm{gC\,m^{-2}}$), as presented in Equation1. The CO_2 fluxes caused by the plant, GPP, and $Rauto$ are computed using Equations 2 and 10, respectively.

$$GPP = Rg \cdot \epsilon_c f_T(Ta) \cdot f_w(WC) \cdot ELUE \cdot APAR \cdot SR10 \tag{2}$$

where Rg is the incoming global radiation ($\mathrm{MJ\,m^{-2}d^{-1}}$), $f_T(Ta)$ is the temperature stress function that depends on Ta the mean air temperature at 2 m (°C), $f_w(WC)$ is the water stress function where WC is the soil water content ($\mathrm{m^{-3}m^{-3}}$). In this study, the water budget is computed but the water stress function is deactivated (*i.e.,* $f_w(WC)$ = 1). In Equation 2, $ELUE$ ($\mathrm{gC\,MJ^{-1}\,m^{-2}}$) is the effective light use efficiency (Equation 3).

$$ELUE = LUE_a + e^{(\frac{Rdiff}{Rg} \cdot LUE_b)} \tag{3}$$

where LUE_a ($\mathrm{gC\,MJ^{-1}\,m^{-2}}$) is the light use efficiency for direct radiation and LUE_b is a correction coefficient for the impact of diffuse radiation Rdiff ($\mathrm{MJ\,m^{-2}d^{-1}}$) on $ELUE$.

In Equation 2, $SR10$ accounts for the decrease in photosynthetic efficiency during senescence linked among others to the decrease in chlorophyll.

$$SR10 = \frac{GLAI}{GLAI\_max \times Cs} \quad if \quad SMT > Sen_a. \quad else \quad SR10 = 1 \tag{4}$$

where Cs is the parameter that controls the slope of $SR10$ depending on the thermal age of the crop SMT and Sen_a refers to the thermal age at which the plant enters senescence. Finally, $FAPAR$ is the fraction of absorbed photosynthetically active radiation and is computed in SAFYE-CO2 (Equation 5).

$$FAPAR = \epsilon_c \cdot 1 - e^{Kex*GLAI} \tag{5}$$

where ϵ_c is the parameter that quantifies the fraction of photosynthetically active radiation in Rg.

SAFYE-CO2 derives $GLAI$ (Equation 6) and other phenotypic traits using allometric coefficients and the plant's organ biomass values such as DAM, Dry Leaf bioMass DLM, and Dry Belowground bioMass DBM (Equation7). To compute these biomass values, the model relies on partition coefficients that dispatch the carbon and resulting biomass in different organs depending on the thermal age of the crop (Equation 8, Baret et al. (1992)).

$$\begin{cases} \Delta GLAI^{+} = DLM \cdot SLA \\ \Delta GLAI^{-} = GLAI \cdot (SMT - Sena) \cdot Senb^{-1} \end{cases} \tag{6}$$

where SLA ($\mathrm{m}^2\,\mathrm{g}^{-1}$) is the specific leaf area and $Senb$ is the rate of functional leaf loss depending on thermal age.

$$\begin{cases} \Delta DAM = \frac{NPP}{Cveg} \cdot (1 - PRT\_R) \\ \Delta DLM = \Delta DAM \cdot (PRT\_L) \\ \Delta DBM = \frac{NPP}{Cveg} \cdot (PRT\_R) \end{cases} \tag{7}$$

where $Cveg$ is the average fraction of carbon in plant biomass.

$$\begin{cases} PRT\_R = PRT\_Rb + (PRT\_Ra - PRT\_Rb) \cdot e^{(-PRT\_Rc \cdot \frac{SMT}{SMT\_G})} \quad if \quad PRT\_R > 0 \quad else \quad PRT\_R = 0 \\ PRT\_L = 1 - PRT\_La \cdot e^{PRT\_Lb \cdot SMT} \quad if \quad PRT\_L > 0 \quad else \quad PRT\_L = 0 \end{cases} \tag{8}$$

The fraction of biomass allocated bellowground PRT_R is computed using PRT_Ra, PRT_Rb, PRT_Rc, and SMT_G which correspond to the end-of-cycle fraction of biomass allocated below-ground, the initial fraction of biomass allocated belowground, a coefficient modulating the decrease in biomass partition to the roots between the initial and end-of-cycle states, and the sum of the temperature at which grain filling starts respectively. The fraction of above-ground biomass allocated to the leaves PRT_L is computed using PRT_La and PRT_Lb0, respectively, the initial fraction of the above-ground biomass that is not allocated to the leaves and a fitting parameter that modulates the rate and thus the end of allocation of above-ground biomass to the leaves.

The biomass and yield are used to determine carbon exports in Equation 1. Equation 9 illustrates a simple way to estimate exported biomass by taking into account only the dry above-ground biomass (DAM), the harvest index (HI), and the fraction of carbon in the dry biomass (Cveg).

$$C_{exports} = \overbrace{DAM \times HI}^{\text{dry Yield}} \times Cveg \tag{9}$$

The other component of NPP, $Rauto$, is divided into vegetation maintenance respiration $Rmaint$ (Amthor, 2000) and vegetation growth respiration $Rgrow$ (Choudhury, 2000) as described in Equation 10.

$$\begin{cases} Rauto = Rmaint + Rgrow \quad where: \\ Rmaint = R10 \cdot Q10^{-0.1\cdot(T-10)} \cdot SR10 \quad and, \\ Rgrow = (1-Yg)\cdot(GPP - Rmaint) \end{cases} \tag{10}$$

$Rmaint$ depends on two parameters: the basal plant respiration at 10 °C ($R10$), temperature sensitivity of plant respiration ($Q10$), and the temperature T and $SR10$ to represent an increase in relative maintenance cost during senescence. The growth respiration is computed from the growth conversion efficiency, GPP, and $Rmaint$.

The final term in NEE, Rh ($\mathrm{gC\,m^{-2}}$) is computed using the empirical model in (Delogu et al., 2017) that depends on soil moisture and temperature.

$$\begin{cases} Rh = Rh_1 \cdot e^{(Rh_2 \cdot T_{soil})} \cdot H_{water-stress} \quad where: \\ H_{water-stress} = (1 + Rh_1 \cdot e^{(Rh_2 \cdot RSM1)})^{-1} \end{cases} \tag{11}$$

Rh_1 is the reference Rh rate, Rh_2 expresses the RH sensitivity to temperature, and H_{water_stress} is the effect of soil moisture on soil carbon decomposition. In H_{water_stress}, Rh_H1 and Rh_H2 provide the form of the water stress function and $RSM1$ the relative soil moisture.

A Python implementation of SAFYE-CO2 was developed for AgriCarbon-EO and is used in this paper. This new version is vectorized to provide predictions for multiple runs and build LUTs. It can also handle multiple vegetation cycles for each run (e.g. crop and cover crop) and has a modular architecture. The physical modules are restructured to regroup soil processes, plant phenology, plant physiology, heterotrophic activity, and field management.

In SAFYE-CO2, the water flux computation is based on the Penman-Monteith and FAO-56 methodologies that enable the computation of evapotranspiration and water distribution in the soil based on a bucket model (Allen et al., 1998). The coupling between the carbon and water cycles occurs in two ways. Plant growth impacts root water uptake, and the soil water content impacts GPP production through a water stress coefficient. The dynamic computation of $GLAI$ in Equation 6 provides the link between the model and the $GLAI$ retrieved from optical EO and therefore allows us to constrain the model's phenological and light use efficiency parameters ($emerg$, PRT_La, PRT_Lb, SLA, $sena$, $senb$, $Harv$, $LUEa$) using EO data assimilation. The assimilation of GLAI allows implicit accounting of soil stress impacts (e.g., nutrients and water) on vegetation development. Therefore,the water stress effect on GPP and plant development is implicitly accounted for through the model's parameters, resulting mainly in lower values of LUE for a field experiencing water stress. Assimilating $GLAI$ also enhances the estimation of NEE and the export of specific organs and the resulting $NECB$ (Equations 9 and 1) by considering the effect of the crop growth dynamic. In data assimilation, the relative parsimony of SAFYE-CO2 compared to models such as STICS (Dumont et al., 2014) or DSSAT (Porter et al., 2010) entails a limited number of free parameters controlling the vegetation dynamics. This, allows the use of scalable assimilation algorithms such as "BASALT" presented below that can only be applied to relatively low dimensional optimization problems (Bellman, 2015).

2.4 Bayesian normalized importance SAmpling using Look out Table - BASALT

To provide large-scale high-resolution assimilation, a tailored inversion method was developed. The new approach, BASALT, relies on the Bayesian normalised importance sampling (NIS) approach to adress the need for uncertainty propagation across the processing chain, and the generation of look-up tables (LUT) provides computational gain by reducing the total number of model simulations. In a Bayesian framework, the initial knowledge about the model's parameters is represented by a probability distribution $P(\Theta)$, the prior distribution. The knowledge brought by the observations x is expressed by the conditional probability distribution $P(\Theta|x)$ of the model parameters knowing the observations x; the so-called posterior distribution. The goal is to evaluate this posterior distribution using Bayes theorem that connects $P(\Theta|x)$, $P(\Theta)$, and $P(x|\Theta)$ called the likelihood (Equation 12)

$$P(\Theta|x) = \frac{P(x|\Theta)P(\Theta)}{P(x)} \tag{12}$$

$P(x)$ is the probability of observation (marginal distribution). Bayesian methods are at the root of popular inversion algorithms such as MCMC or Dream (Vrugt, 2016). Such algorithms have often been applied to agronomic modelling (Dumont et al., 2014), ecosystem modelling (Ma et al., 2022), and radiative transfer modelling (Zhang et al., 2005).

In BASALT, random samples are generated for the model according to the probability distribution that best represents the user's prior knowledge of the model's parameters. The model output variables are calculated for each of those samples, given forcing and fixed parameters specific to a spatial and/or temporal range. The sampled parameters and resulting variables are treated as an LUT containing the prior state of the model for the range where the forcing is valid. Following LUT creation, the different LUT entries are compared against observations with known uncertainty. Using a normal error model for the observation allows computing log-likelihoods as presented in Equation 13. Following this step, the relative likelihoods (RL) of each LUT entry can be computed as presented in Equation 14. In AgriCarbon-EO, this can be done for different scales, i.e., the entity scales or at the scale of a group of entities. Finally, the posterior distribution is computed based on the underlying error model with a normal distribution by computing a weighted mean and standard deviation (Equation 15).

$$logL_{i,j} = \sum(-\frac{1}{2}log(2\pi(\sigma_{o,i,j})^2)) - \frac{(v_{o,i,j} - \mu_{o,i,j}^2)}{2\sigma_{o,i,j}} \tag{13}$$

where v is the simulation value, μ and σ are the mean and standard deviation of the observation, j is the index for entities, o is the index of the independent observations, and i is the index for the model run in the LUT.

$$RL_i = \frac{e^{logL_i}}{\sum_i e^{logL_i}} \quad ; \quad RLfield_i = \frac{\sum_k RL_{i,k}}{\sum_i \sum_k RL_{i,k}} \tag{14}$$

where RL_i is the relative likelihood at the entity scale, k are the entities in the same field, and $RLfield_i$ is the relative likelihood at the field scale assuming an equal contribution of each pixel in the field.

$$\mu_w(v_i, RL_i) = \frac{\sum_i v_i RL_i}{\sum_i RL_i} \quad ; \quad \sigma_w(v_i, RL_i, \mu_w) = \frac{\sum_i (v_i - \mu_w)^2 \cdot RL_i}{\sum_i RL_i} \tag{15}$$

where μ_w is the weighted mean, v_x is the vector given by the LUT for a parameter or variable, x is the number of samples and $\sigma_w$is the weighted standard deviation.

2.4.1 Retrieval of GLAI maps from PROSAIL

When inverting PROSAIL, the main objective is to retrieve $GLAI$ and its associated uncertainties that will be assimilated by SAFYE-CO2. This is done by generating an LUT of PROSAIL runs (size = 5000) for each remote sensing image based on the prior (Table 1), and the solar and observation angles provided by Sentinel-2 and Landsat-8 products. Equations (14) are then used to evaluate the RL where j is the index of pixels in the simulated image, i is the index of the PROSAIL runs in the LUT, and o is the observed reflectances from the Sentinel-2 or Landsat-8 images. As PROSAIL provides LAI and not $GLAI$, the chlorophyll content (cab) is constrained to a high interval [60,80] $\mathrm{ug\,m^{-2}}$. This makes all simulated surfaces green and thus allows to retrieve $GLAI$. A constraint is also added to the relation between dry biomass and $GLAI$ to reduce the parameter search space by eliminating solutions with leaves that are too thin or thick. Then, the surface reflectances of the Level 2-A BOA products are considered to follow a normal distribution with a mean and a standard deviation that is fixed at 0.02. Finally, the posterior distribution is approximated with a normal distribution, using Equation 15 to determine μ and σ.

Table 1. Priors configuration for PROSAIL parameters used in the Bayesian inversion.

Name	description	Unit	Prior (uniform [min,max])
N	Leaf structure parameter	.	[1,2]
cab	Chlorophyll a+b concentration	μg m^{-2}	[60,80]
car	Carotenoid concentration	μg m^{-2}	[5,20]
cm	Leaf thickness	g cm^{-2}	[-0.02,0.02] + LAI·0.004
LAI	Leaf area index	m^2 m^{-2}	[0,5]
$psoil$	Soil moisture index	.	[0,1]

2.4.2 Application of BASALT to SAFYE-CO2

The simulated variables, DAM, $yield$, GPP, $Reco$, and NEE, are highly dependent on the duration and intensity of crop development (Ceschia et al., 2010). The $GLAI$ outputs from PROSAIL are assimilated into SAFYE-CO2 to correct the prior vegetation dynamics. This is done by generating an LUT of SAFYE-CO2 runs (size = 5000) for each zone with the same forcing (*i.e.,* same prior). In this case, the zoning is defined by the weather forcing data (*i.e.* SAFRAN at 8 km). For each zone, Equations 13 and 14 are applied to evaluate the RL given the $GLAI$ observations, where j is the index of pixels in the simulated area, i is the index of the SAFYE-CO2 runs in the LUT, and o the observed $GLAI$ at different dates. The priors for LUT generation for SAFYE-CO2 are shown in Table 2. Those priors are used for the SAFYE-CO2 LUT generation and were reassessed in terms of statistical distribution from (Pique et al., 2020a) to account for the high-spatial heterogeneity that can be observed at a regional scale and the vegetation cycles that are more contrasted at the pixel level than at the field level due to the regression to the mean. For each parameter, a truncated normal distribution is independently sampled considering μ, σ, min, and max values; the only exception is PRT_Lb, which has an exponential behaviour. For this parameter, a logarithmic transformation is applied to the distribution. To aggregate the SAFYE-CO2 simulations at the field scale, the likelihood is summed over all the pixels in the field (Equation 14). Finally, Equation 15 is used to compute μ and σ for a parameter or a variable on a given day for a field or pixel.

Table 2. Priors configuration for SAFYE-CO2 parameters used in the Bayesian inversion.

Name	Description	Unit	Prior [μ,σ,min,max]
$emerg$	Day of year of vegetation emergence	DOY	$[335, 15, 200, 400]$
$harv$	Day of year of vegetation harvest	DOY	$[200, 0, 160, 200]$
LUE_a	Light use efficiency	g MJ^{-1}	$[1.05, 0.05, 0.8, 1.5]$
SLA	Specific Leaf Area	m^2 g^{-1}	$[0.01, 0.002, 0.004, 0.05]$
PRT_La	Initial fraction of biomass that is not allocated to the leaves	g g^{-1}	$[0.325, 0.15, 0.01, 0.5]$
PRT_Lb	Decrease rate of the fraction of biomass allocated to the leaves.	g g^{-1} $°C^{-1}$	$[1.01, 0.005, 1, 1.02]$
$sena$	Sum of temperature at which senescence starts	°C	$[1350, 200, 1000, 2000]$
$senb$	Rate of senescence	°C m^2 m^{-2}	$[12000, 3000, 0, 20000]$
HI	Harvest Index	gg^{-1}	$[0.45, 0, 0.45, 0.45]$

3 Application for wheat in Southwest France

3.1 Experimental setup and study area description

Several assimilation experiments were conducted to answer the specific objectives of the paper, they are summarized in Table 3. The experiments correspond to simulations over the Sentinel-2 31TCJ tile located in the southwestern of France for winter wheat in 2017, 2018, and 2019 (Figure 2). They alternate between the use of S2 alone and the combined use of S2 and L8. They also include pixel and field scale simulations. The ACEO-S2L8-Pixel combines Landsat-8 and Sentinel-2 data at 10 m resolution which represents approximately 20 M pixels for our study area. It was used as the main simulation for the validation experiments. The ACEO-S2L8-Field simulations correspond to averaging the 10 m $GLAI$ from PROSAIL retrievals at the field scale. Additionally, an averaging of the high-resolution simulations with Sentinel-2 and Landsat-8 was performed at the field scale (ACEO-S2L8-Mean).

The study area has a mean annual precipitation of 655 mm and a mean annual temperature close to 13 °C. It is classified as a majorly temperate oceanic climate (Cbf) in the plains, and temperate continental climate (Dfb) near the Pyrénnées mountains, based on the Koppen climate classification. In 2017, winter was exceptionally dry and sunny, and spring was sunny with a 10 $\%$ deficit in rainfall (Météo-France, 2019), while 2019, had a mild winter and a sunny spring with 10 $\%$ deficit rainfall for the two seasons (Météo-France, 2021). The region has an intermediary cloud coverage that allows for multitemporal optical remote sensing analysis and analysis of the impact of clouds (Figure 2.B). It is mainly occupied by agricultural fields that

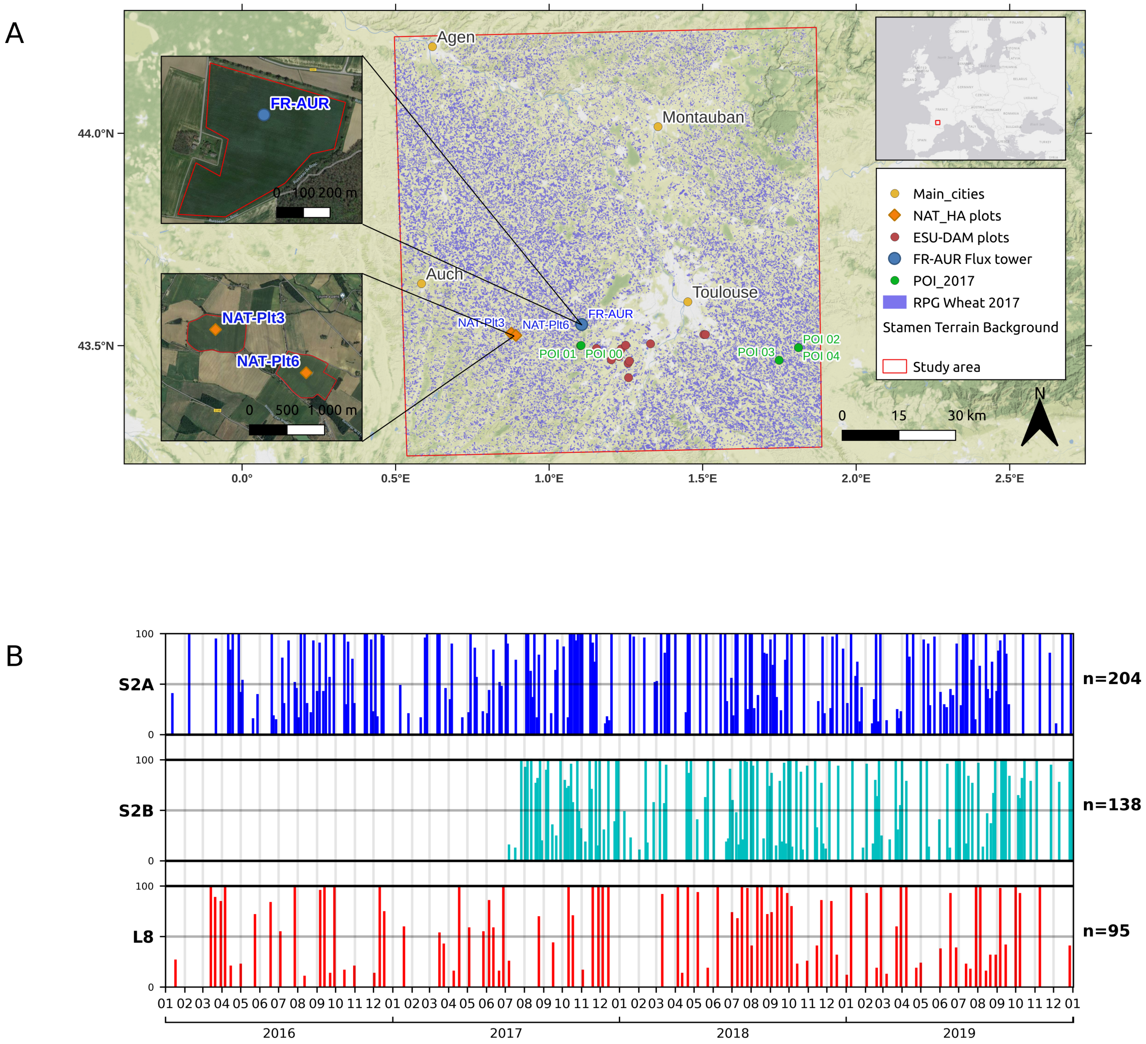

Figure 2. Map of the simulation area and image availability from 2016 to 2019. In "A": background the ESRI World Topo Map, the 31TCJ Sentinel2 tile limits (red rectangle), land cover for winter wheat fields for 2017 (blue), location of the FR-AUR ICOS site, the Dry Above ground Biomass (DAM) measurements (red circles) and the two fields monitored with connected combine harvester (CH) (orange circles). The zoomed maps show the FR-AUR field and the fields monitored using combine harvesters. In "B": Chronogram of the remote sensing dataset from Sentinel-2A (S2A), Sentinel-2B (S2B) and Landsat-8 (L8), over the 31TCJ tile for 2016 to 2019. The bar plots represent the percentage of cloud-free pixels for each image.

Table 3. Name, aim, and inputs details of the assimilation experiment.

Name	Aim	RS Data	Spatial resolution	Years
ACEO-S2-Pixel	- Determine the impact of revisits.	S2	Pixels (10m)	2017
ACEO-S2L8-Pixel	- Validate the model outputs.	S2 & L8	Pixels (10m)	2017,18,19
ACEO-S2L8-Field	- Quantify the impact of spatial resolution.	S2 & L8	Fields*	2017
ACEO-S2L8-Mean	- Quantify the spatial variability.	S2 & L8	Fields**	2017

* for ACEO-S2L8-Field the $GLAI$ from PROSAIL inversion is averaged prior to the SAFYE-CO2.

** for ACEO-S2L8-Mean the outputs at 10m from SAFYE-CO2 are averaged at field scale.

cover approximately 90 % of the area, among which a majority of seasonal crops. Winter wheat covers approximately 20 % of the zone and reaches 40 % in some areas. In South-West France, soft-wheat varieties are predominant, and they are usually sown in autumn around mid to end of October. Soft wheat represents 75 % of the French exports of soft wheat. The crop typically develops slowly during the winter, and growth accelerates during spring. It is harvested from mid-June to the end of July depending on maturation as well as climatic conditions to optimize grain. The harvest in 2017 was normal (6 $\mathrm{t\,ha^{-1}}$ at 15 % humidity), while 2019 was an exceptional year with a yield of 11.5 $\mathrm{t\,ha^{-1}}$ at 15 % humidity (ARVALIS, 2019). In terms of pedology, two main soil types are present in the area of study: silt-rich soils near the major streams, and clay soils across the hills with a variable density of stones depending on erosion. The topography offers a wide range of aspects. The region also bears the effects of historical land management, specifically, the “Remembrement” policy, a political push to merge adjacent fields from 1945 to 1980 in France (Baker, 1961). This leads to a wide range of soil and microclimatic conditions that cause significant intrafield plant growth variability.

This study area was chosen for three main reasons in light of the aims of the paper. First, it is part of the Space Regional Observatory that benefits from extensive datasets regarding crop growth and crop physiology through the presence of two certified ICOS flux sites (FR-AUR and FR-LAM), and extensive measurement campaigns operated by different public laboratories specializing in agronomy and remote sensing as well as measurement campaigns operated by private companies and individual farmers. These measured variables related to the field’s carbon budget such as NEE, GPP, $Reco$, DAM, and $Yield$ (Equations 1 and 9) are monitored in different localities with different representative scales (Table 3.2). Second, the crop growth and biophysical process variability, due to topography and pedo-climatic variations, is needed to assess the impact of using high-resolution modelling and assimilation schemes in quantifying the carbon budget components (e.g. $Yield$, $\mathrm{CO_2}$ fluxes). Third, winter wheat is one of the most studied crops worldwide. This allows us to compare the quality of the results obtained with AgriCarbon-EO against a large corpus of published studies. Furthermore, the area is a dense crop production zone. This is especially true for wheat production, which has a large economic interest.

3.2 Validation of the AgriCarbon-EO outputs

The validation relies on several datasets corresponding to the main output variables of AgriCarbon-EO: CO_2 flux measurements (*i.e.* NEE, GPP, $Reco$), DAM measurements over Elementary Sampling Units (ESU), and yield maps. A summary of the ID and characteristics of the aforementioned validation datasets is presented in Table 4. The validation datasets were extracted from the database of the Environmental Information System maintained by the CESBIO laboratory (SIE, 2022).

Table 4. Description of the validation data sets.

ID	Source	Type	Sampling	Scale	Frequency
FR-AUR C-Flux	ICOS	GPP, Reco, NEE	Eddy covariance	FR-AUR field	Daily
FR-AUR DAM	ICOS	DAM	FR-AUR field	10 m	During and at end of cycle *
ESU-DAM	RSO	DAM	8 ESU	10 m	1 to 4 dates during the cycle *
NAT-HA	farmer	Yield	2 CH at two fields	30 cm	At end of cycle

* The list of dates is provided in supplemental materials.

3.2.1 Validation against field scale CO_2 fluxes and DAM measurements

The FR-AUR ICOS site provides many biophysical measurements, among which variables of interest regarding the carbon budget GPP, $Reco$ and NEE (FR-AUR C-Flux, Table 4). These variables allow us to assess the soundness of the representation of CO_2 fluxes caused by physiological processes in the model, as GPP represents photosynthesis and $Reco$ the sum of plant and soil respiration. Furthermore, NEE allows access to the representation of the biological part of the carbon budget and DAM is linked to carbon export (Equation 9) and NPP (Equation 1). As one of the requirements for the ICOS certification is the homogeneity of the ecosystem, the measurements were considered to be representative of the field. The DAM and CO_2 flux measurements were acquired using the ICOS destructive biomass sampling protocol (Gielen et al., 2018) and eddy covariance (EC) flux tower measurements processed with EdiRe software (Clement, 2008), following the CarboEurope-IP recommendations for data filtering, quality control, and gap filling (Table 4). The EC method consists of measuring the 3D wind fluctuations at 20 hz using a high-frequency sonic anemometer and the CO_2 concentration using a gaz analyser. The covariance is then computed between the turbulent component of the vertical wind and the turbulent component of the CO_2 concentrations (Baldocchi, 2003). The NEE was then partitioned into GPP and Reco using a formulation for croplands in Béziat (2009) adapted from (Reichstein et al., 2005). Depending on wind speed and the intensity of the turbulence, a fraction of the direct measurements are not representative of the plot, and those data points were filtered out during the processing and replaced with simulated values extrapolated from the environmental conditions. We maintained only daily data points where more than 50% of the information comes from real measurements, as gap-filling over long periods induces high errors (Béziat, 2009). The days when less than 50% of the information is provided by measurements are represented in grey in Figure 3. Furthermore, it is also noticeable that the observed $Reco$ in 2018-2019 dips to zero during the vegetation growth period, which is related to an error in the partitioning process of NEE into GPP and $Reco$. This period is also ignored for GPP and $Reco$ and is represented in red in Figure 3.

In this exercise, the daily outputs from AgriCarbon-EO at 10 m resolution were spatially averaged over the area of the FR-AUR field (Equation 14) sampled by the EC tower (a.k.a. the target area in the ICOS nomenclature). Those averaged values were then compared against FR-AUR DAM and FR-AUR C-Flux as shown in Figure 3, and the corresponding fitting statistics are shown in Table 5. The statistics were computed for three specific periods, from the 1^{st} Jan to the 1^{st} May, the 1^{st} May to the 1^{st} Jul, and the 1^{st} Oct to the 1^{st} Oct. These periods correspond to the growing and senescence of the wheat crop and the whole cropping year respectively. The $GLAI$ fitting statistics computed over the growing season show a good fit (R^2 = 0.95) in 2016-2017 with a slightly lower fit in 2018-2019 (R^2 = 0.91). From mid-November 2018 until the end of January 2019, spontaneous regrowth of the previous crop (i.e., rapeseed) was observed in the field. The model does not reproduce this $GLAI$ dynamic, as this increase does not correspond to the wheat crop cycle. The $GLAI$ for 2018-2019 senescence period is underestimated by the model.

Regarding observed as well as simulated DAM, end-of-cycle values are higher for the 2019 cropping year than in 2017, which is consistent with regional yield statistics (ARVALIS, 2019). additionally, the modeled aboveground biomass dynamics are consistent with the observed dynamics, apart from an overestimation of the simulation at the beginning of the vegetation cycle in 2017. Note that replicates in 2016-2017 and 2018-2019 present a noticeable spread. In 2017, the dynamics of the $\mathrm{CO_2}$ fluxes are well represented with most of the observed values in the uncertainty margin of the model with R^2 values of 0.87, 0.91, and 0.76 for NEE, GPP, and $Reco$, respectively. The model's daily flux variations are slightly higher than the observations in 2017. In 2019, the $\mathrm{CO_2}$ flux dynamics are less well reproduced, nevertheless with acceptable R^2 values (above 0.7) over the full year. For the cropping year R^2 was 0.77, 0.79, and 0.70 for NEE, GPP, and $Reco$ respectively. The modelled GPP values are significantly higher than the observed values during the growing period (bias = 3.31 $\mathrm{gC\,m^{-2}}$), while the differences between the model and observations are less pronounced at the end of the vegetation cycle (bias = -0.87 $\mathrm{gC\,m^{-2}}$).

3.2.2 Validation against spatialised DAM measurements

The ESU protocol allows the assessment of variables at decametric scales. Among those variables DAM is especially of interest as it can be used as a proxy for NPP (Equation 7). Moreover, the exported yield can be computed using end-of-cycle biomass. (Equation 9). To measure DAM with the ESU protocol, the above-ground vegetation is sampled at five points following a cross pattern inscribed in a 10 × 10 m square; each sample corresponds to one linear meter of the crop row. The five samples are weighed fresh in the field. In the laboratory, one of the five samples is dried to retrieve the canopy water content, which is then applied to the five fresh weight measurements to obtain dry above-ground biomass. The mean and standard deviation are computed to obtain a representative DAM ($\mathrm{g\,m^{-2}}$) for the ESU. Eight fields were sampled using the ESU protocol in 2018 and simulations were performed for each ESU (Supplemental Materials).

Figure 4 shows the scatter plot between the simulated and observed DAM colored with respect to the month of acquisition for 8 fields with up to four revisits. The statistics corresponding to this figure are recorded in Table 6. The comparison shows a

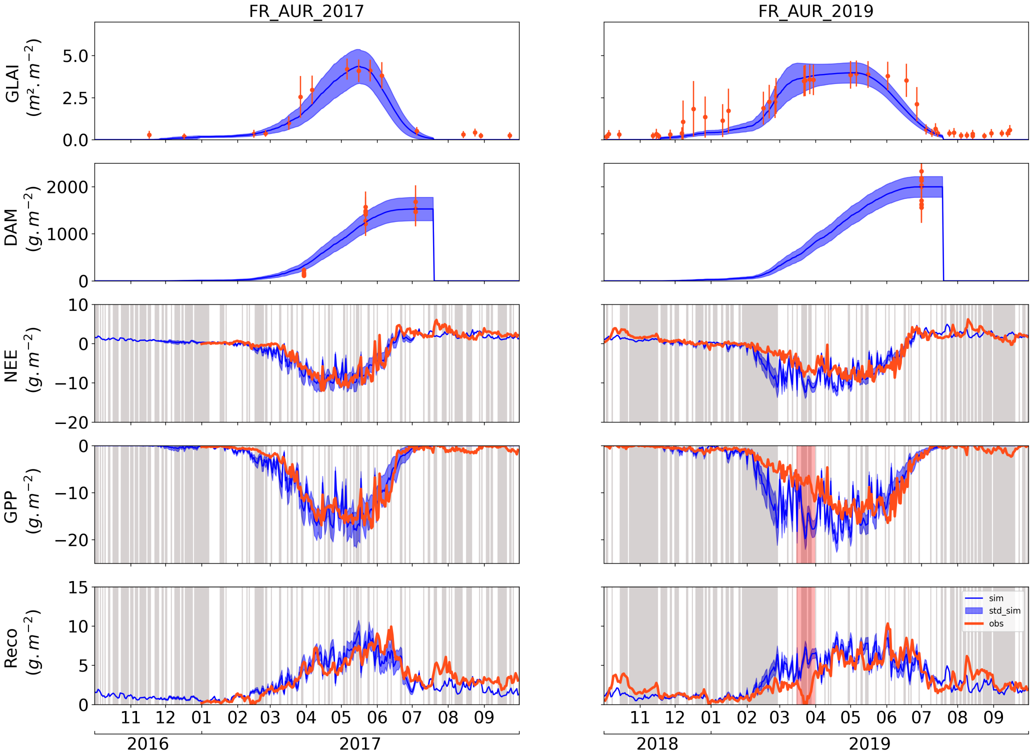

Figure 3. Time series of $GLAI$, DAM, NEE, GPP and $Reco$. The blue line and surface represent the mean and standard deviation of the posterior distribution. The orange points with error bars represent the $GLAI$ derived from the satellite observations and the DAM, NEE, GPP, and $Reco$ at the FR-AUR site for two cropping years (2016-2017 and 2018-2019). In the case of the $\mathrm{CO_2}$ fluxes, the grey areas represent the days during which more than 50% of the data are gap-filled, and the red area represents the periods during which a partitioning error has been identified.

good fit when considering all DAM measurements with an R^2 of 0.94, an RMSE of 211.34 $\mathrm{g\,m^2}$ and a mean overestimation of the model of 129 $\mathrm{g\,m^{-2}}$. These statistics represent the spatiotemporal fitting of the model.

When analysing the statistics per month, it is noticeable that most of the total bias is present at the early growth stages (in April) and the bias decreases over the growing season. The final DAM values linked to yield and carbon exports in July have low bias, and we canexplain 61 % of the variability. In addition, a weaker correlation is present when the data are split per month compared to the full dataset (Table 6). The variability in a given month is mainly due to the spatial variability. Splitting the data thus enables us to assess the variability in the spatial and temporal components that are simulated by AgriCarbon-EO. Given the small sample size, these monthly results should be interpreted with caution.

Table 5. Bias, R^2 and RMSE statistics for $GLAI$, DAM, GPP, $Reco$ and NEE variables in FR-AUR site over years 2017 and 2019 for the growth and senscence and cropping year.

Variable	Statistic	2017			2019		
		Growth	Senescence	All	Growth	Senescence	All
	Bias	0.36	0.19	0.27	0.21	0.44	0.35
GLAI	RMSE	0.63	0.39	0.45	0.51	0.71	0.56
$(\mathrm{m}^2\,\mathrm{m}-2)$	R2	0.92	0.95	0.95	0.96	0.87	0.91
	Bias	-	-	-6.46	-	-	4.78
DAM	RMSE	-	-	172.34	-	-	380.62
$(\mathrm{g}\,\mathrm{m}-2)$	R2	-	-	0.97	-	-	-
	Bias	0.43	0.13	0.28	2.39	-0.86	0.62
NEE	RMSE	1.52	2.04	1.68	3.42	1.90	2.38
$(\mathrm{g}\,\mathrm{m}-2)$	R2	0.86	0.87	0.87	0.64	0.87	0.77
	Bias	0.78	-0.53	0.03	3.31	-0.87	0.67
GPP	RMSE	1.87	2.06	1.82	4.67	2.26	3.00
$(\mathrm{g}\,\mathrm{m}-2)$	R2	0.92	0.91	0.91	0.75	0.87	0.79
	Bias	-0.35	0.66	0.25	-0.91	0.01	-0.12
Reco	RMSE	0.80	1.38	1.13	1.32	1.40	1.29
$(\mathrm{g}\,\mathrm{m}-2)$	R2	0.88	0.69	0.76	0.84	0.50	0.70

Table 6. Values of RMSE, MAE, Bias and R^2 between the simulated and observed Dry Above ground bioMass (DAM).

Dataset	Bias $(\mathrm{g}\,\mathrm{m}^{-2})$	RMSE $(\mathrm{g}\,\mathrm{m}^{-2})$	R^2
April	-281.80	286.19	0.65
May	-76.18	116.46	0.89
July	17.37	222.43	0.61
all	-129.44	211.34	0.94

3.2.3 Comparison with high resolution combine harvester yield maps

Yield maps are of high interest for the evaluation of high-resolution crop models in the context of carbon and precision farming. They provide information on the grain yield that often represents the bulk of the carbon that is exported from the field. CH are also the only readily available spatial and direct high-resolution crop organ monitoring tools. Nevertheless, they have

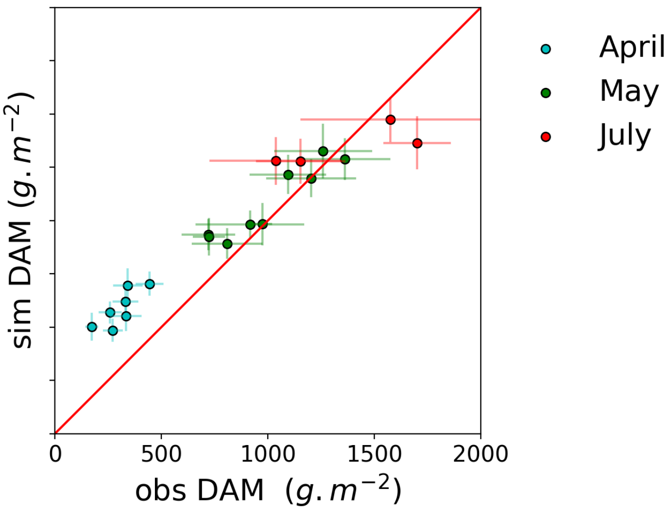

Figure 4. Scatter plot of the simulated winter wheat dry aboveground biomass (DAM) versus the observed biomass in the fields in 2018.

drawbacks because the mass flow sensor and the grain moisture content sensor can experience significant sensor drift within the field. Moreover, CH yield data processing requires a range of parameters such as lag time settings and distance travelled via GPS measurements, header position, and cut width, all of which contribute to the uncertainty in the measurements (D. Grisso et al., 2002). In this study, yield CH data were provided by a farmer located in the Gers département. Data from two fields NAT-Plt3 and NAT-Plt6 (Table 4), were collected by a CH that measures the incoming flow of grain, its humidity, and its position at a fixed frequency with a GPS. These measurements were integrated between two points of the trajectory taking into account harvesting width to compute the grain production (yield) per surface area. The grain humidity content enabled the computation of the dry yield mass ($\mathrm{g\,m^{-2}}$). The point yield data is then converted into a harvest map over the simulation grids by summing the points inside each pixel. A Gaussian smoothing filter with sigma = 12 m was then applied over these maps to reduce the aliasing effects. The spatial anomaly (*i.e.* $(value - \mu)/\sigma$) maps were also computed. To complete the processing, the colocalization error between observations and AgriCarbon-EO yield estimates was minimized through the detection of the maximum spatial correlation in a 10 m lateral shift range.

The simulated yield maps were obtained from the ACEO-S2L8-Pixel simulation by multiplying the final DAM by HI (Equation 9). We analysed the results in terms of the retrieval of the spatial patterns as shown in Figure 5. These maps show the comparison between the CH yield data and the AgriCarbon-EO yield estimates at the pixel level in $\mathrm{t\,ha^{-1}}$ as well as the spatial yield anomaly. Overall the observed yields show a larger variability than the simulations and a clear saturation effect is observed in the simulations for the NAT-plt6 field. The AgriCarbon-EO and CH anomaly maps show clear spatial patterns. However, the spatial patterns are more pronounced over the NAT-Plt3 field than over NAT-Plt6. RMSEs of 0.70 and 0.68 $\mathrm{t\,ha^{-1}}$, biases of 0.42 and 0.41 , and R^2 values of 0.12 and 0.29 are observed for NAT-Plt3 and NAT-Plt6, respectively. The performances of the yield simulations vary strongly between the two fields. A relatively low RMSE and bias indicate a quite good mean representation of the plots. However, the correlation coefficient is quite low and indicates that not all the spatial variability in yield can be captured using this approach. The small R^2 can however be explained by the range of variation in wheat yield that is smaller at intra-field scale than regional scale. In fact, maximum R^2 values of 0.32 and 0.22 are found when assuming an observation measurement error of $1\ \mathrm{t\,ha}^{-1}$ (Supplemental Materials). Furthermore, if we compare these simulations to standard fieldwise simulations that do not explain spatial variability, the explained spatial variance illustrated here is a net gain. Difficulties in reproducing the range of yield observed variations in yield values may be caused by the simple representation of grain biomass allocation through the use of an HI which does not take into account potential variations in the HI due to nutrient availability or crop cycle duration (Dai et al., 2016).

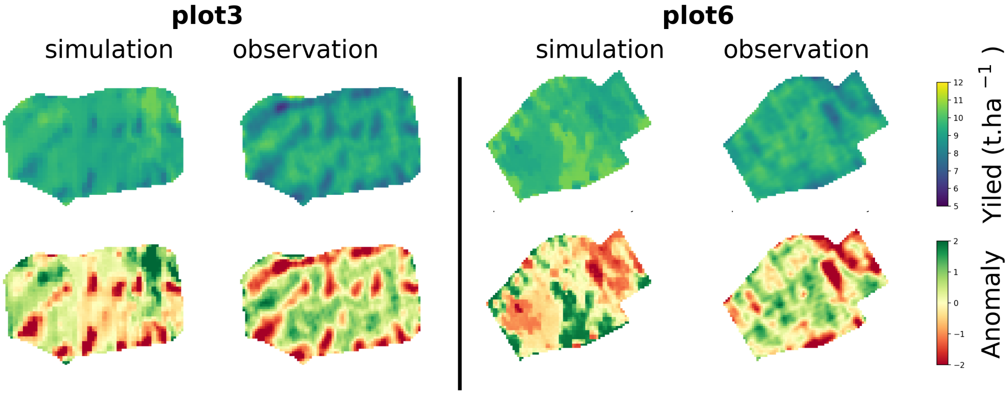

Figure 5. Yield maps and spatial anomalies simulated by AgriCarbon-EO and collected using a combine harvester over the Nataïs site (NAT-Plt3 and NAT-Plt6) for 2017 and 2019.

3.3 Large scale simulation outputs

In this section, the results from the ACEO-S2L8-Pixel in 2017 are illustrated and analysed. The RPG land cover map for winter wheat fields, the SAFRAN weather data, and the THEIA S2 and L8 EO data were used as input along with the parametrization files for PROSAIL and SAFYE-CO2. The AgriCarbon-EO processing chain was run in parallel over a single server rack with 2 computation nodes and with 36 threads max. The memory requirement was the highest for the PROSAIL retrievals, reaching $5\ \mathrm{Gb}$ per process (image inversion) for a LUT size of 5000. For SAFYE-CO2 the requirements were 5 Gb per process with one process per node of the weather grid with a LUT size of 5000. A SAFYE-CO2 run over the $110 \times 110\ \mathrm{km}$ area of study at 10 m resolution required 4 hours of computation time per year of simulation. The chain was able to produce maps of all parameters and variables estimated by SAFYE-CO2. With the carbon budget being our main priority here, we chose to focus on NEP, DAM at the end of the vegetation cycle, $Cexport$ (Equation 9), and $NECB$ (Equation 1). The NEP was computed by summing NEE over one cropping year from 1^{st} Oct 2016 to 30^{th} Sep 2017. Maps of NEP, $Cexport$, and $NECB$ at native resolution $(10\ \mathrm{m})$ are shown in Figure 6(A) as an illustration of typical outputs from the chain. The histograms of the same variables and their uncertainty are shown in Figure 6 (B). Note that, in these figures, we presented NEP and $NECB$ in the soil-oriented convention (i.e., positive values mean net $\mathrm{CO_2}$fixation and soil organic carbon storage, respectively) to be able to compare the values of NEP, $Cexport$, and $NECB$.

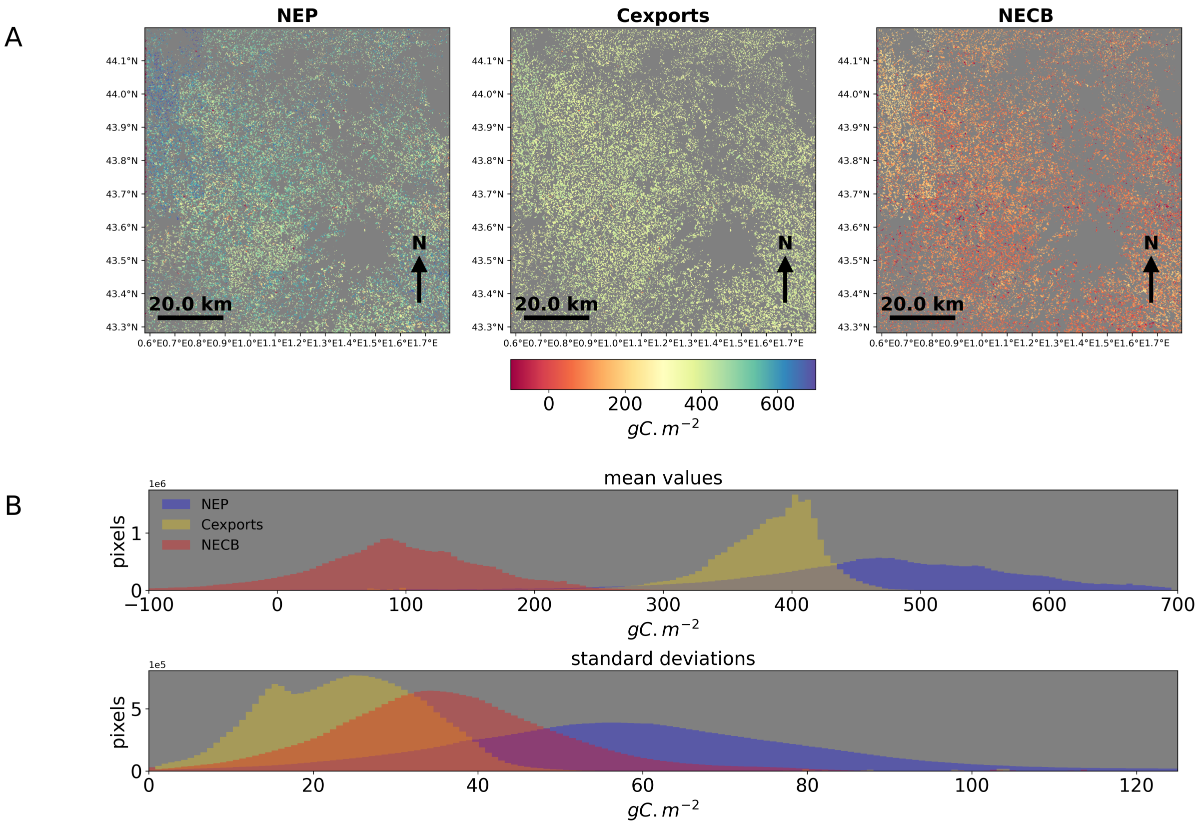

Figure 6. Regional scale carbon budget outputs from AgriCarbon-EO assimilation using S2 and L8. In "A": From left to right, NEP, $Cexport$ (yield), and $NECB$ for the winter wheat fields for the 2016-2017 cropping season. In "B": the histogram of the posterior mean and standard deviation of the same variables on top and bottom, respectively. Note that NEP and $NECB$ are presented in the soil-oriented convention. Positive values of NEP and $NECB$ thus correspond to net annual $\mathrm{CO_2}$ sinks and soil organic carbon storage, respectively.

High levels of heterogeneity with regional patterns can be seen in the retrieved simulations. The northwestern and southeastern corners are characterized by higher CO2 fixation and thus growth, yield, and lower $NECB$. The variability of NEP is mostly comprised between 300 and 700 $\mathrm{gC\,m^{-2}}$, which is consistent with eddy covariance measurements for wheat across Europe (Ceschia et al., 2010). Furthermore, the dry yield varies between 6.6 $\mathrm{t\,ha^{-1}}$ (i.e 300 $\mathrm{gC\,m^{-2}}$) and 10 $\mathrm{t\,ha^{-1}}$ (i.e., 450

$\mathrm{gC\,m^{-2}}$), which is also coherent with regional statistics (ARVALIS, 2019). In Figure 6 negative values of NEP and $NECB$ correspond to pixels where wheat did notdevelop. In those cases, Rh dominates during the cropping year, leading to a net carbon loss in the soil.

The uncertainty, (i.e. standard deviation of the posterior distribution) has mean values of 55, 25, and 38 $\mathrm{gC\,m^{-2}}$ for NEP, $Cexport$, and $NECB$, respectively. The spatial variability (i.e. standard deviation of the mean pixel values) is equal to 131, 50 and 82 $\mathrm{gC\,m^{-2}}$ for those same variables. The fact that the uncertainty is lower than the retrieved spatial variability indicates that this method has enough resolution to discriminate and ordinate values of NEP, $Cexport$, and $NECB$ based on the update of priors using remote sensing-based $GLAI$. However, the fact that those values are on the same order of magnitude stresses that uncertainty assessments should always be provided with these analyses. The maps and distributions, given their scale and resolution, do not showcase the full range of crop variability that can be observed in the study area. To illustrate individual solutions and anomalies encountered in the simulations selected pixels of interest (POIs, located in Figure 2) are presented in Figure 7 .

These pixels are selected to illustrate intrafield heterogeneity and specific anomalies. Figure 7 (a-e) shows in green the $GLAI$ inverted using PROSAIL with their respective uncertainties, and the simulated $GLAI$ time series in red with a higher transparency for the solutions with the lowest contribution (likelihood). For instance, the results in Figure 7 (a) POI-00 and (b) POI-01 show the fitting of the model over two pixels in the same field. It is clear from the observed and the $GLAI$ between the two POIs that the vegetation phenology is different, with early emergence and higher maximum $GLAI$ in the case of POI-00 (a) and later emergence and lower maximum $GLAI$ in the case of POI-01 (b). Additionally, Figure 7 (c) POI-02 and (d) POI-03 are adjacent pixels in the same field, but each is on a different side of a cloud mask in May 2017. The input $GLAI$ from PROSAIL on this date is associated with very low uncertainty, which impacts the retrieval of the SAFYE-CO2 model. The low uncertainty will result in a high level of false information for this date, which In turn will negatively impact the Bayesian inversion and reduce the SAFYE-CO2 model performances, thereby pushing the model to better fit this unrealistic inversion of $GLAI$. Finally, Figure 7 (e) POI-04 corresponds to a pixel in a field where the observed $GLAI$ is not consistent with winter wheat; in fact, this $GLAI$ dynamic fits better to a summer crop such as sunflower. Mislabeling in the land cover such as this one can result in “no fitting”. Mislabeled winter crops could, however, be fitted and not stand out in the spatialized simulation.

3.4 Impact of the spatial resolution and temporal sampling of assimilated GLAI

The AgriCarbon-EO simulations (Table 3) were compared at different scales (*i.e.* pixel vs. field) and for different satellite image temporal densities to investigate the benefit of assimilating high-resolution multimission derived $GLAI$ into SAFYE-CO2. The impact of the spatial scale of the $GLAI$ assimilation is illustrated by Figure 8 (a), which shows the histogram of ($DAM_{\mathrm{ACEO-S2L8-Pixel}}$ - $DAM_{\mathrm{ACEO-S2L8-Field}}$). An average negative bias of -47 $\mathrm{g\,m^{-2}}$ is observed for DAM with a spread between -210 $\mathrm{g\,m^{-2}}$ and +120 $\mathrm{g\,m^{-2}}$ for the $[-\sigma, +\sigma]$ interval when comparing the pixel scale simulation to the field scale simulation. This result is interpreted as the bias error that can be avoided by applying an intrafield assimilation scheme in the crop model in contradiction to the more generally applied field scale. Note that the same bias value is obtained for Figure 8 (b), representing the difference between the averaged pixel at field scale and the field scale simulations:

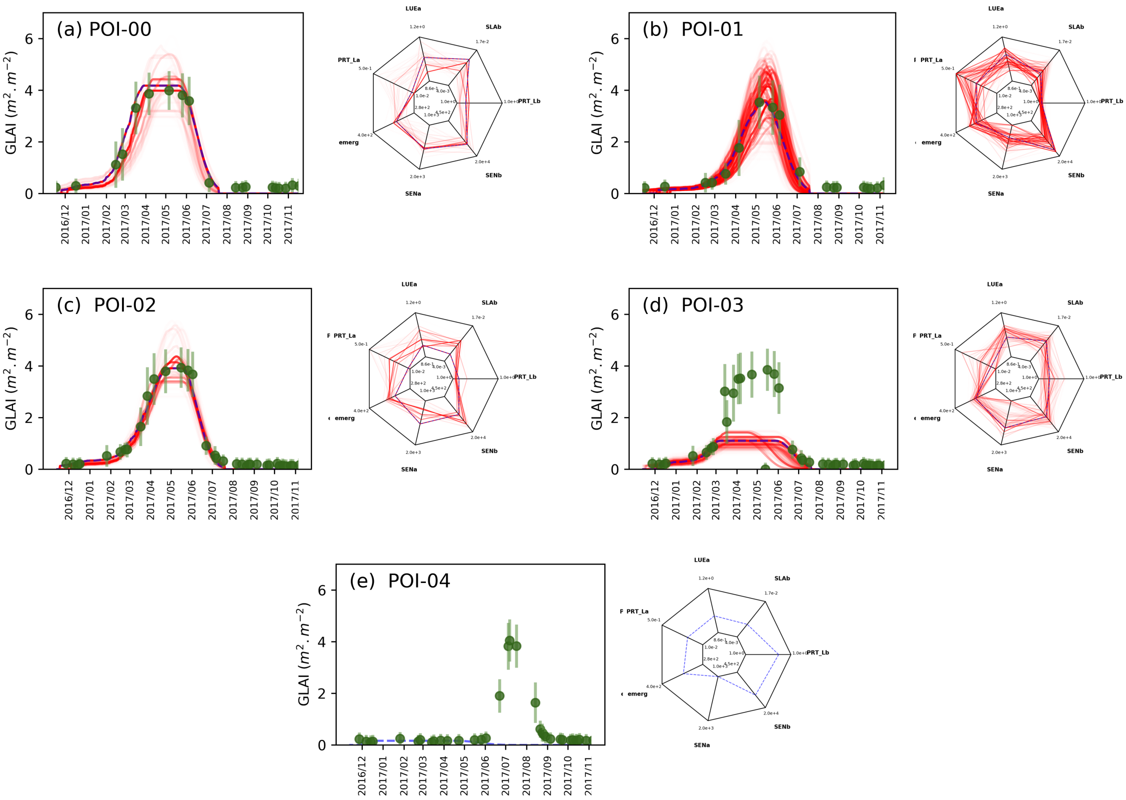

Figure 7. Time series of $GLAI$, and radar plots containing the free parameters of SAFYE-CO2. Simulations are represented in red with a transparency proportional to their relative likelihood and the maximum likelihood simulation is represented in blue dashed lines. POI-00 (a) and POI-01 (b) are located in the same field. POI-02 (c) and POI-03 (d) are adjacent pixels where a cloud date is not filtered in (d). POI-04 (e) illustrates either an error in the CAP declaration or a failed wheat crop followed by a summer crop .

($DAM_{\mathrm{ACEO-S2L8-Mean}}$ - $DAM_{\mathrm{ACEO-S2L8-Field}}$). This is mathematically expected as $DAM_{\mathrm{ACEO-S2L8-Mean}}$ is obtained by averaging the $DAM_{\mathrm{ACEO-S2L8-Pixel}}$ simulations. However, when comparing the RMSE values between Figure 8 (a) and (b) a noticeable change in RMSE of -68 $\mathrm{g\,m^{-2}}$ is observed. This result shows that the variability of simulated biomass will decrease by 39 % when considering field-scale modelling. The variability is directly influenced by the retrieved parameters of the crop model between the intrafield and field scales for the same crop cycle; resulting in a different posterior parameter distribution, as shown in the section above. Figure 8 (c) shows the difference between a simulation using only S2 and using S2 + L8. Adding L8 images tends to slightly increase dry biomass, with a bias of 30 $\mathrm{g\,m^{-2}}$ and an RMSE of 94 $\mathrm{g\,m^{-2}}$. This difference is caused by the additional samples added at the start and end of the vegetation cycle that result in a change in the length of the vegetation cycle.

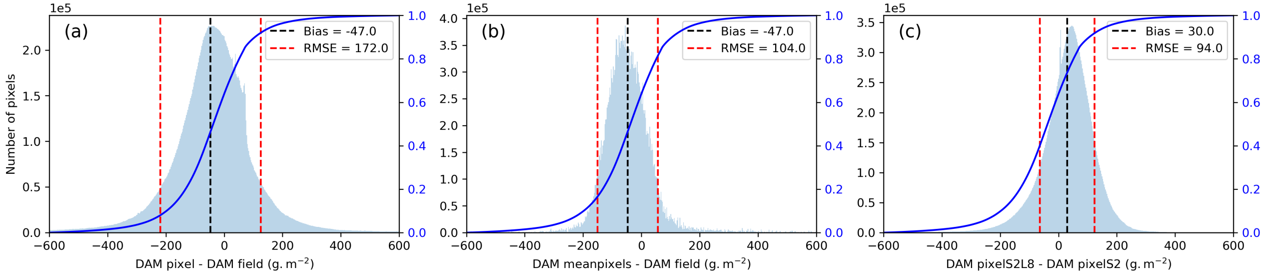

Figure 8. Histogram (left y-axis) and cumulative density function (right y-axis) of the bias of biomass at harvest (y-axis). (a) corresponds to ($DAM_{\mathrm{ACEO-S2L8-Pixel}}$ - $DAM_{\mathrm{ACEO-S2L8-Field}}$), (b) ($DAM_{\mathrm{ACEO-S2L8-Mean}}$ - $DAM_{\mathrm{ACEO-S2L8-Field}}$) and (c) ($DAM_{\mathrm{ACEO-S2L8-Pixel}}$ - $DAM_{\mathrm{ACEO-S2-Pixel}}$).

To assess the robustness of the assimilation approach given a variable number of assimilated images, the DAM outputs from ACEO-S2L8-Pixel were analysed in terms of the number of images over each pixel. Figure 9 shows the impact of the number of $GLAI$ observations per pixel on μ and σ of the DAM. σ of DAM decreases by approximately 66 % with the number of observations (146 $\mathrm{g\,m^{-2}}$ for 11 images to 48 $\mathrm{g\,m^{-2}}$ for 28 images) while the μ DAM values remain stable. This illustrates the stability of μ values given the range of variation of observed images. However, the decrease in σ also illustrates the contribution of the number of images to the constraining of solutions and increased accuracy.

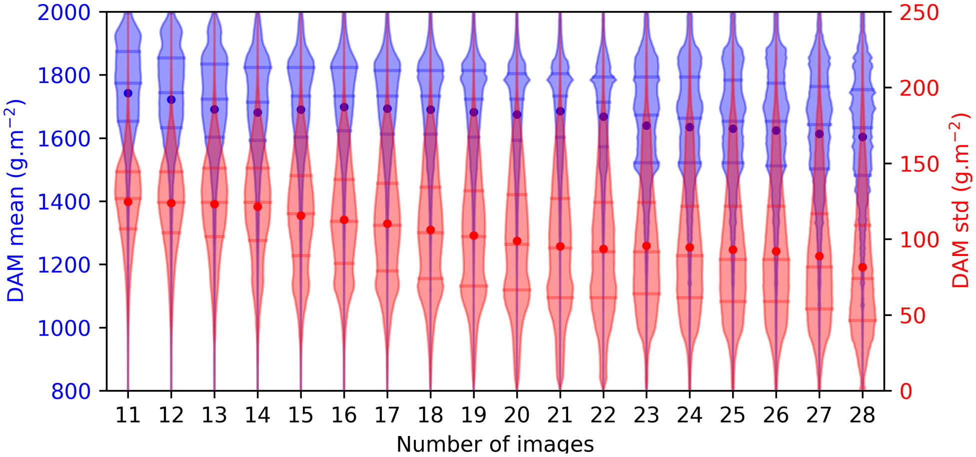

Figure 9. Violin-plots of the number of images used for the inversion over each pixel on the x-axis and the mean (μ) DAM on the right y-axis and the standard deviation (σ) of DAM on the left y-axis.

4 Discussion

4.1 Quality of carbon budget component retrieval

To contextualize the performance of the retrieval of the carbon budget components simulated by AgriCarbon-EO, we compare the results obtained in our study against recent and relevant studies that evaluate at least one of the components that are showcased in this study. Concerning the evaluated variables, the performances are in the range of the scores observed in previous validation exercises with SAFYE-CO2 at the field scale (Pique et al., 2020a). When compared to other models, Combe et al. (2017) constrained the WOFOST agronomic model with 25 km resolution yield and sowing date data, over 3 ICOS sites comparable to FR-AUR, across Europe. This dataset represents 10 site-year combinations in total. They obtained R^2 values ranging from 0.64 to 0.74, and RMSE values ranging from 2.33 to 2.67 $\mathrm{g\,m^{-2}}$ for NEE over wheat fields. The values we retrieved for FR-AUR (Table 5) are higher regarding R^2 and on the low end of values obtained for RMSE, indicating the potential added value of high-resolution agronomic diagnostics. In the same study, GPP was also evaluated and R^2 and RMSE values going from 0.82 to 0.87 and 2.33 to 2.83 $\mathrm{g\,m^{-2}}$were found. The R^2 retrieved from AgriCarbon-EO is slightly higher, and the RMSE was in the same range for 2019 and lower for 2017. The GPP was also analysed using WOFOST at 25 km resolution by assimilating GPP values derived from the MODIS satellite's observations in Zhuo et al. (2022). In this study, the GPP values were evaluated over 2 years against a flux tower measurement site in Oklahoma (USA). They obtained R^2 values of 0.87 and 0.67 and RMSE values of 2.26 and 3.25 $\mathrm{g\,m^{-2}}$ in 2015 and 2016, respectively. These values are in the same range as the GPP retrieved by AgriCarbon-EO. The $Reco$ is rarely evaluated by models, as it implies simulating plant and soil processes simultaneously. Combe et al. (2017) retrieved $Reco$ with R^2 values ranging from 0.76 to 0.83 and RMSE values ranging from 0.98 to 1.29 $\mathrm{g\,m^{-2}}$. The R^2 obtained with AgriCarbon-EO is slightly lower and the RMSE slightly higher than in (Combe et al., 2017) for $Reco$. Zhuo et al. (2022), cited before, also evaluated DAM time series measured at the same flux tower site with RMSE= 121 and 81 $\mathrm{g\,m^{-2}}$ and R^2 =0.94 and 0.93. These statistics concern the whole cropping cycle and can thus be compared against Table 6 for the "all" item and the DAM statistics regarding FR-AUR 2017. AgriCarbon-EO shows a similar variation as in Zhuo et al. (2022). In Tewes et al. (2020), in-situ LAI is assimilated into the LINTUL5 crop model using NIS. The estimations of DAM obtained at maturity (BBCH 99) were compared against field measurements collected on 14 plots located in the Netherlands, northern France, and Germany (from 40 to 60 in-situ sampling points representative of 1 m^2), showing a mean RMSE of 246 $\mathrm{g\,m^{-2}}$ and a mean bias of 58 $\mathrm{g\,m^{-2}}$. These results can be compared to the end-of-cycle biomass measurements retrieved using AgriCarbon-EO that yield similar performances using $GLAI$ derived from satellite measurements in Table 6. Regarding yield, which is often the main focus of studies on agronomic modelling, more references are available. Among these, Tewes et al. (2020), retrieves a mean RMSE= 170 $\mathrm{g\,m^{-2}}$, Bias = -27 $\mathrm{g\,m^{-2}}$ and Hao et al. (2021) presents a meta-analysis of 76 studies using the APSIM model, that is broadly used for wheat yield simulations for which the conclude that an RMSE = 100 $\mathrm{g\,m^{-2}}$ is expected. The RMSE retrieved by AgriCarbon-EO is in the same range as these studies. However, for a more accurate evaluation of wheat yield performance, a larger number of yield maps with a larger range of variation should be analysed, and better modelling of yield needs to be integrated as the current version is based on a simple multiplicative harvest index.

To summarize, the AgriCarbon-EO processing chain allows the retrieval of the carbon budget components with performances that are close to or better than existing state-of-the-art evaluations. Nevertheless, the performance of AgriCarbon-EO should be evaluated in other pedo-climatic conditions by taking advantage in particular of the data provided through the regional Fluxnet, ICOS, and Ameriflux networks to confirm this statement.

Furthermore, not needing input data such as crop calendars, cropping practices, or variety-specific information for simulating the biomass and the $\mathrm{CO_2}$ fluxes makes this approach unique. However to calculate the NECB, farmer data relative to organic amendments and straw harvesting are needed. It is also notable that most of the studies cited here perform low-resolution analysis in plains, where the spatial variability is expected to be low. The same approaches may be penalized when applied to areas with high spatial variability, such as the hilly countryside in southwestern France. Our bibliographical research yielded no other studies that perform simulations that are specific to crop growth at a decametric resolution using agronomic models of the previously mentioned variables while covering large areas in the 100 by 100 km range.

4.2 Multimission data, cloud cover, and limitations

The retrieval of SAFYE-CO2 parameters and of the carbon budget components in AgriCarbon-EO relies on the accuracy and availability of EO data, which is hampered by errors in image colocation, atmospheric corrections, the presence of clouds, and cloud shadow correction. Many studies show that these effects have an important impact on agricultural remote sensing applications such as yield estimation (Soriano-González et al., 2022), land cover (Song et al., 2021), and superficial soil carbon content mapping (Vaudour et al., 2019). In our study, we show that these effects are mitigated through the use of a Bayesian approach in a multitemporal context because the uncertainty in the EO-derived $GLAI$ is accounted for in the assimilation process. Our approach shows that increasing the number of observations does not strongly impact the mean DAM values, but increases its uncertainty by approximately 66 $\%$. Nevertheless, unfiltered clouds or the lack of images significantly impact the simulations locally (Figure 7 (c)). This means that improvements in cloud detection algorithms will highly benefit our approach (Skakun et al., 2022). The analysis of $GLAI$ time series to detect anomalous variations (Figure 7 (d)) could also be an option to filter clouds. Furthermore, the use of additional data from Landsat-8 enhanced the simulation quality for our region of interest. Finally, additional optical or even biophysical variables retrieved from synthetic aperture radar (SAR) satellite data could mitigate the loss of data due to cloud cover in northern and coastal regions (Veloso et al., 2017; Fieuzal et al., 2017).

4.3 Impact of remote sensing and input spatial-resolution

Intrafield heterogeneity is a well-established issue in agricultural applications (Weiss et al., 2020; Blackmore et al., 2003; Grieve et al., 2019; Nowak, 2021). However, it has not been thoroughly treated in terms of $\mathrm{CO_2}$ fluxes and uncertainty estimates. In this paper, we argue that reliable and accurate estimates of DAM and $\mathrm{CO_2}$ fluxes in support of carbon budget component monitoring require intrafield scale estimates. Our results show that by assimilating mean-field level $GLAI$ products in SAFYE-CO2 a bias of -47 $\mathrm{g\,m^{-2}}$ and an artificial relative uncertainty decrease of 39 $\%$ on DAM will be induced compared to assimilating high-resolution $GLAI$ and calculating the mean of the model's output. High resolution thus allows more accurate estimates of the mean DAM values at the field scale, which in turn also enables more accurate field-scale estimates of SOC changes by soil models. Nevertheless, the use of even higher-resolution remote sensing data may be relevant to address carbon budget components at very small or elongated fields, such as those in rural India (Deininger et al., 2017). The other input data products that drive the spatial resolution of the AgriCarbon-EO outputs are the land cover and the weather data. While the land cover is available at an adequate resolution (*i.e.* field sale), it is error-prone, either because of erroneous CAP declarations (Magnin, 2019) or because of classification errors when EO-based land cover maps are used (Liu et al., 2022). Interestingly, our results show that when a mismatch occurs, the fields in question exhibit high anomalies in retrieved parameters and are thus detectable. For the weather forcing, the current application was based on the Météo-France 8 km resolution Safran data, which provides reasonable accuracy over France (Garrigues et al., 2015). Currently, ECMWF provides ERA5-Land at $0.1°$ resolution globally (Muñoz-Sabater et al., 2021), and NOAA provides weather reanalysis at 3 km over the US (Dowell et al., 2022). In the future, the coverage and resolutions of weather-forcing data are expected to increase (*i.e.* ERA6 at 2.5 km). Increasing the resolution of the weather forcing in AgriCarbon-EO would provide better spatial information but would also increase the computational demand by a factor of γ as the LUT for SAFYE-CO2 is generated over the weather grid (Equation 16).

$$\gamma = \frac{TLUT \times 8^2}{\theta^2} \tag{16}$$

$TLUT$ is the processing time for the generation of LUT and θ is the weather grid resolution in km.

4.4 Limitations of the Bayesian and physically based approach

While the components of AgriCarbon-EO have been tailored to the requirements mentioned in the introduction (large scale, high resolution, uncertainty estimates, and biophysical processes), we have shown limits for each of them. For instance, the BASALT Bayesian approach can be sensitive to an erroneous observation associated with low uncertainty (Figure 7 d). A trade-off must be made between the variability of the generated solutions, and the number of LUT entries to maintain computational efficiency. A solution could be to consider a joint distribution for prior parameters to propose a better ratio of appropriate solutions (Wang et al., 2022). On the one hand, radiative transfer modelling is constrained by the spectral library database (Verhoef et al., 2007), which may not reflect ground conditions such as the presence of weeds impacting $GLAI$ retrievals. On the other hand, the crop model predictions will depend on fixed and prior parameters of a given crop. Alternatively, we could have reverted to machine learning approaches that have gained popularity for precision agriculture and soil carbon farming applications (Sharma et al., 2021). However, while they are powerful tools, they need a large amount of training data to take into account climatic conditions and management practices and need to be updated regularly as we encounter unprecedented weather conditions. Hybrid solutions such as AgriCarbon-EO that combine parsimonious process-based modeling and remote sensing approaches are thus needed. In the current state, it is reasonable to consider that an MRV platform for SOC carbon stock changes should include an ensemble of approaches with varying levels of complexity (e.g. Tier 1,2 and 3) (Nevalainen et al., 2022), similar to what has been implemented in the IPCC approaches (Parker, 2013). In this framework, AgriCarbon-EO is designed to be a Tier 3 MRV approach for crop carbon farming.

4.5 From AgriCarbon-EO to SOC budget

The present approach provides high-resolution estimates of key carbon budget components and estimation of $NECB$ and SOC variations. To achieve this, the SAFYE-CO2 crop model currently uses a simplified soil respiration module that simulates Rh without modelling the different carbon pools in the soil (Equation 11). This methodology is adapted for short-term assessment of carbon budgets (typically up to one year) (Pique et al., 2020a). This means that stock-dependent soil processes that affect SOC mineralization and litter humification that may cause priming effects are not accounted for here. The inclusion of a soil carbon decomposition module, as in Guenet et al. (2016), that includes such processes would allow a better representation of soil respiration and account for the effect of amendments with different decomposition dynamics. Such an exercise, would however increase the number of parameters and create the need for the addition of in situ or spatial map datasets to provide initial soil carbon content, soil chemical characteristics, and organic amendment information. Procurement at a large scale of such information with sufficient accuracy is still challenging for large-scale applications. One way of achieving this is to take advantage of the rapidly developing Farm's Management Information Systems (FMIS) and enhanced soil property maps through digital soil mapping (DSM). Even though farmer activity data are not easily accessible, it is expected that this limitation will be reduced with the development of soil carbon farming policies (such as the Label Bas Carbone in France) and auditing schemes (de Gruijter et al., 2016). Such data exchange would have a dual positive effect, provided that adequate soil sampling protocols are applied. The SOC data would increase the size of existing datasets available for validation and verification of tools like AgriCarbon-EO, and at the same time, approaches such as AgriCarbon-EO may provide optimal sampling strategies for the estimation of SOC stock changes for carbon auditing.

5 Conclusion

The main aim of the paper is to present the AgriCarbon-EO processing chain that assimilates remote sensing data into the PROSAIL radiative transfer model and the SAFYE-CO2 crop model to estimate key carbon budget components of crop fields at high resolution and regional scale. AgriCarbon-EO was designed to cover essential features to comply with the monitoring component of the MRV systems for cropland carbon budget (Smith et al., 2020; Paustian et al., 2019):

1. Provide a scalable solution, which is of major specification in the design of AgriCarbon-EO. The proposed assimilation scheme has been constructed to prevent the time-related drawbacks of iterative methods while enabling easy integration of additional information.

2. Provide the component of the carbon budget (biomass and carbon fluxes) with their associated uncertainties. The uncertainty of the model's variables is estimated using an innovative Bayesian approach labelled BASALT.

3. Estimate the carbon budget at intrafield resolution. High-resolution modelling is enabled by the assimilation of EO data at a 10 m resolution, which is a coherent resolution with verification data and provides the means to determine optimal in-situ soil and vegetation sampling.

4. Propose a preoperational tool, that uses and facilitates access to remote sensing, weather, and ancillary data in an end-to-end processing chain.

The paper details the mathematical concepts and the algorithm behind the AgriCarbon-EO processing chain. The use of a noniterative Bayesian NIS methodology (BASALT) in AgriCarbon-EO has enabled to overcome high computational needs. Validation and analysis have been performed using an application over winter wheat crop in South-West France. Our results show that when validating the simulations against flux tower measurements, we find that the new inversion approach (BASALT) produces reliable estimates of $\mathrm{CO_2}$ fluxes (NEE, GPP, and $Reco$) and performs similarly to SAFYE-CO2 in previous studies while providing uncertainty estimates. Our estimates for DAM are close to the observations while the validation exercise for yield is less conclusive due to the small range of yield values, the uncertainty of the CH's data and processing, and/or the use of a HI to estimate yield that may not account for essential drivers of yield. Our analysis of the impact of the number of remote sensing acquisitions shows a reduction in uncertainty of 66 % when full S2 and L8 data are available, while the median retrieved NEE and DAM remained the same. This points to the stability of the method in this range of satellite observation availability. Furthermore, we find that the assimilation of field scale $GLAI$ products induces a bias on the DAM from -120 to 210 $\mathrm{g\,m^{-2}}$ and a reduction in the DAM interfield variability of about 39 % compared to pixel scale assimilation. Based on this, we argue that an intrafield scale quantification of the carbon budget components $NECB$ is preferable as this resolution provides 1) coherent spatial information with soil samples. 2) the means to provide better sampling strategies for soil and plant monitoring approaches. Further applications of AgriCarbon-EO will enable the extension of such analysis to other crops, cover crops, and climatic conditions. Several limitations were identified in the discussion about AgriCarbon-EO. Primary enhancement should concern the addition of a soil carbon pool model into the soil module to take into account long-term changes in the carbon stock, the integration of information from farm management databases (FMIS) to better account for organic amendments and configure the carbon exports, and finally enhancing the accuracy of the assimilation scheme by integrating additional remote sensing data such as SAR. Finally, from the broader perspective of agronomic modelling, it should be noted that AgriCarbon-EO can also provide variables related to the water cycle such as soil moisture, evaporation, transpiration, and drainage. It can thus be envisioned as a coherent agronomic decision support tool for yield, phenology, carbon, and water fluxes.

Author contributions. TW and AA proposed the methodology. TW, AA, and LA developed the chain code. TW and AA conducted the simulations and the visualizations. TW, AA, and EC conducted the analysis. EC and AA provided funding acquisition and supervision. TW and AA prepared the manuscript. EC, LA, and RF provided comments on the manuscript. All authors agreed on the proposed paper.

Competing interests. The contact authors declare that neither they nor their coauthors have any competing interests.

Acknowledgements. Data acquisition at FR-Aur was mainly funded by the Institut National des Sciences de l'Univers of the Centre National de la Recherche Scientifique (CNRS-INSU) through the ICOS and OSR SW observatories. We thank Franck Granouillac, Tiphaine Tallec, Jean-François Dejoux, and Nicole Claverie for their technical support. We extend special thanks to Mr. Andréoni (farmer) for accommodating measurement devices in their fields at FR-AUR. T. Wijmer's thesis was financed by the NIVA project from ASP and "Naturellement Popcorn". Financial support was also obtained from the ERANET ANR SMARTIES project, the Horizon Europe ClieNfarm (n° 101036822) and ORCaSa (n° 101059863) projects, and the Bag'ages (Agence de l'eau Adour Garonne) projects. This work was granted access to the HPC resources of the CALMIP super-computing center under the allocation 2022-P20013.

Code and data availability. The source of datasets and codes is given hereafter.

Datasets:

1. Remote sensing data for Sentinel-2 and Landsat8 using the maja processing are downloaded from THEIA: https://www.theia-land.fr/en/product/senti 2-surface-reflectance/. The Sentinel-2 level 2A and Landsat8 L2A data are distributed under the ETALAB V2.0 open license.
2. Land Cover datasets are available at : https://geoservices.ign.fr/rpg
3. Validation datasets are available from the SIE website : https://sie.cesbio.omp.eu/
4. Full dataset of all simulations is about 5T of memory, selected outputs can be made available upon request to the authors.
5. Output maps for wheat 2017 are available at: 10.5281/zenodo.7534280

Code availability:

AgriCarbon-EO is implemented in python3. AgriCarbon-EO requires the PROSAILv5 python package and the SAFYE-CO2 v2.0.5 python implementation. AgriCarbon-EO v1.0.1 is available free of charge for research and evaluation purposes (non-commercial) upon signature of a licence agreement with the Toulouse Technology Transfer (TTT) office of Université Toulouse 3.

For this, the user contacts the TTT at "contact@toulouse-tech-transfer.com" providing contact information, affiliation, and objective of use. Upon validation of the license, the code is provided by the team at CESBIO. SAFYE-CO2 v2.0.5 is provided with AgriCarbon-EO v1.0.1 in this same procedure. Note that for this paper, and in compliance with the journal requirements, an anonymous procedure was put in place to grant access to the reviewers. PROSAIL: python bindings v2.0.3 for PROSAIL5 is hosted at https://github.com/jgomezdans/prosail and archived under https://zenodo.org/record/2574925#.Y-lIVK3MI2w by Dr.José Gómez-Dans.

References

Allen, R. G., Pereira, L. S., Raes, D., and Smith, M.: Crop evapotranspiration - Guidelines for computing crop water requirements - FAO Irrigation and drainage paper 56, Tech. rep., FAO, 1998.

Amthor, J. S.: The McCree–de Wit–Penning de Vries–Thornley Respiration Paradigms: 30 Years Later, Annals of Botany, 86, 1–20, https://doi.org/10.1006/anbo.2000.1175, https://doi.org/10.1006/anbo.2000.1175, 2000.

ARVALIS: ARVALIS : Toute l'info pour gérer son exploitation agricole, https://www.arvalis-infos.fr/index.html, 2019.

Baetens, L., Desjardins, C., and Hagolle, O.: Validation of Copernicus Sentinel-2 Cloud Masks Obtained from MAJA, Sen2Cor, and FMask Processors Using Reference Cloud Masks Generated with a Supervised Active Learning Procedure, Remote Sensing, 11, 433, https://doi.org/10.3390/rs11040433, https://www.mdpi.com/2072-4292/11/4/433, number: 4 Publisher: Multidisciplinary Digital Publishing Institute, 2019.

Baker, A. R. H.: LE REMEMBREMENT RURAL EN FRANCE, Geography, 46, 60–62, https://www.jstor.org/stable/40565215, publisher: Geographical Association, 1961.

Baldocchi, D. D.: Assessing the eddy covariance technique for evaluating carbon dioxide exchange rates of ecosystems: past, present and future, Global Change Biology, 9, 479–492, https://doi.org/10.1046/j.1365-2486.2003.00629.x, http://onlinelibrary.wiley.com/doi/abs/10.1046/j.1365-2486.2003.00629.x, _eprint: https://onlinelibrary.wiley.com/doi/pdf/10.1046/j.1365-2486.2003.00629.x, 2003.

Baret, F., Jacquemoud, S., Guyot, G., and Leprieur, C.: Modeled analysis of the biophysical nature of spectral shifts and comparison with information content of broad bands, Remote Sensing of Environment, 41, 133–142, https://doi.org/10.1016/0034-4257(92)90073-S, https://www.sciencedirect.com/science/article/pii/003442579290073S, 1992.

Battude, M., Al Bitar, A., Brut, A., Tallec, T., Huc, M., Cros, J., Weber, J.-J., Lhuissier, L., Simonneaux, V., and Demarez, V.: Modeling water needs and total irrigation depths of maize crop in the south west of France using high spatial and temporal resolution satellite imagery, Agricultural Water Management, 189, 123–136, https://doi.org/10.1016/j.agwat.2017.04.018, https://www.sciencedirect.com/science/article/pii/S0378377417301609, 2017.

Bellman, R. E.: Adaptive Control Processes: A Guided Tour, in: Adaptive Control Processes, Princeton University Press, https://doi.org/10.1515/9781400874668, https://www.degruyter.com/document/doi/10.1515/9781400874668/html, 2015.

Blackmore, S., Godwin, R. J., and Fountas, S.: The Analysis of Spatial and Temporal Trends in Yield Map Data over Six Years, Biosystems Engineering, 84, 455–466, https://doi.org/10.1016/S1537-5110(03)00038-2, https://www.sciencedirect.com/science/article/pii/S1537511003000382, 2003.

Bolinder, M. A., Crotty, F., Elsen, A., Frac, M., Kismányoky, T., Lipiec, J., Tits, M., Tóth, Z., and Kätterer, T.: The effect of crop residues, cover crops, manures and nitrogen fertilization on soil organic carbon changes in agroecosystems: a synthesis of reviews, Mitigation and Adaptation Strategies for Global Change, 25, 929–952, https://doi.org/10.1007/s11027-020-09916-3, https://doi.org/10.1007/s11027-020-09916-3, 2020.

Béziat, P.: Effets des conditions environnementales et des pratiques culturales sur les flux de carbone et d'eau dans les agrosystèmes, phdthesis, Université Paul Sabatier - Toulouse III, https://tel.archives-ouvertes.fr/tel-00447499, 2009.

Ceschia, E., Béziat, P., Dejoux, J. F., Aubinet, M., Bernhofer, C., Bodson, B., Buchmann, N., Carrara, A., Cellier, P., Di Tommasi, P., Elbers, J. A., Eugster, W., Grünwald, T., Jacobs, C. M. J., Jans, W. W. P., Jones, M., Kutsch, W., Lanigan, G., Magliulo, E., Marloie, O., Moors, E. J., Moureaux, C., Olioso, A., Osborne, B., Sanz, M. J., Saunders, M., Smith, P., Soegaard, H., and Wattenbach, M.: Management effects on net ecosystem carbon and GHG budgets at European crop sites, Agriculture, Ecosystems & Environment, 139, 363–383, https://doi.org/10.1016/j.agee.2010.09.020, https://www.sciencedirect.com/science/article/pii/S0167880910002537, 2010.

Chapin, F. S., Woodwell, G. M., Randerson, J. T., Rastetter, E. B., Lovett, G. M., Baldocchi, D. D., Clark, D. A., Harmon, M. E., Schimel, D. S., Valentini, R., Wirth, C., Aber, J. D., Cole, J. J., Goulden, M. L., Harden, J. W., Heimann, M., Howarth, R. W., Matson, P. A., McGuire, A. D., Melillo, J. M., Mooney, H. A., Neff, J. C., Houghton, R. A., Pace, M. L., Ryan, M. G., Running, S. W., Sala, O. E., Schlesinger, W. H., and Schulze, E.-D.: Reconciling Carbon-cycle Concepts, Terminology, and Methods, Ecosystems, 9, 1041–1050, https://doi.org/10.1007/s10021-005-0105-7, https://doi.org/10.1007/s10021-005-0105-7, 2006.

Choudhury, B. J.: A sensitivity analysis of the radiation use efficiency for gross photosynthesis and net carbon accumulation by wheat, Agricultural and Forest Meteorology, 101, 217–234, https://doi.org/10.1016/S0168-1923(99)00156-2, https://www.sciencedirect.com/science/article/pii/S0168192399001562, 2000.

Clement, R.: EdiRe Software for Micrometeorological Applications, 2008.

Clivot, H., Mouny, J.-C., Duparque, A., Dinh, J.-L., Denoroy, P., Houot, S., Vertès, F., Trochard, R., Bouthier, A., Sagot, S., and Mary, B.: Modeling soil organic carbon evolution in long-term arable experiments with AMG model, Environmental Modelling & Software, 118, 99–113, https://doi.org/10.1016/j.envsoft.2019.04.004, https://www.sciencedirect.com/science/article/pii/S1364815218307643, 2019.

Combe, M., de Wit, A. J. W., Vilà-Guerau de Arellano, J., van der Molen, M. K., Magliulo, V., and Peters, W.: Grain Yield Observations Constrain Cropland CO2 Fluxes Over Europe, Journal of Geophysical Research: Biogeosciences, 122, 3238–3259, https://doi.org/10.1002/2017JG003937, https://onlinelibrary.wiley.com/doi/abs/10.1002/2017JG003937, _eprint: https://onlinelibrary.wiley.com/doi/pdf/10.1002/2017JG003937, 2017.

D. Grisso, R., J. Jasa, P., A. Schroeder, M., and C. Wilcox, J.: YIELD MONITOR ACCURACY: SUCCESSFUL FARMING MAGAZINE CASE STUDY, Applied Engineering in Agriculture, 18, 147, https://doi.org/10.13031/2013.7775, https://elibrary.asabe.org/abstract.asp?aid=7775&t=3, place: St. Joseph, MI Publisher: ASAE, 2002.

Dai, J., Bean, B., Brown, B., Bruening, W., Edwards, J., Flowers, M., Karow, R., Lee, C., Morgan, G., Ottman, M., Ransom, J., and Wiersma, J.: Harvest index and straw yield of five classes of wheat, Biomass and Bioenergy, 85, 223–227, https://doi.org/10.1016/j.biombioe.2015.12.023, https://www.sciencedirect.com/science/article/pii/S0961953415301951, 2016.

de Gruijter, J. J., McBratney, A. B., Minasny, B., Wheeler, I., Malone, B. P., and Stockmann, U.: Farm-scale soil carbon auditing, Geoderma, 265, 120–130, https://doi.org/10.1016/j.geoderma.2015.11.010, https://www.sciencedirect.com/science/article/pii/S0016706115301269, 2016.

De Jong, J.: Een karakterisering van de zonnestraling in Nederland, Technische Hogeschool Eindhoven, Eindhoven, 1980.

Deininger, K., Monchuk, D., Nagarajan, H. K., and Singh, S. K.: Does Land Fragmentation Increase the Cost of Cultivation? Evidence from India, The Journal of Development Studies, 53, 82–98, https://doi.org/10.1080/00220388.2016.1166210, https://doi.org/10.1080/00220388.2016.1166210, publisher: Routledge _eprint: https://doi.org/10.1080/00220388.2016.1166210, 2017.

Delogu, E., Le Dantec, V., Mordelet, P., Ceschia, E., Aubinet, M., Buysse, P., and Pattey, E.: Improved methodology to quantify the temperature sensitivity of the soil heterotrophic respiration in croplands, Geoderma, 296, 18–29, https://doi.org/10.1016/j.geoderma.2017.02.017, https://www.sciencedirect.com/science/article/pii/S0016706117302677, 2017.

Dowell, D. C., Alexander, C. R., James, E. P., Weygandt, S. S., Benjamin, S. G., Manikin, G. S., Blake, B. T., Brown, J. M., Olson, J. B., Hu, M., Smirnova, T. G., Ladwig, T., Kenyon, J. S., Ahmadov, R., Turner, D. D., Duda, J. D., and Alcott, T. I.: The High-Resolution Rapid Refresh (HRRR): An Hourly Updating Convection-Allowing Forecast Model. Part 1: Motivation and System Description, Weather and Forecasting, -1, https://doi.org/10.1175/WAF-D-21-0151.1, https://journals.ametsoc.org/view/journals/wefo/aop/WAF-D-21-0151.1/WAF-D-21-0151.1.xml, publisher: American Meteorological Society Section: Weather and Forecasting, 2022.

Drusch, M., Del Bello, U., Carlier, S., Colin, O., Fernandez, V., Gascon, F., Hoersch, B., Isola, C., Laberinti, P., Martimort, P., Meygret, A., Spoto, F., Sy, O., Marchese, F., and Bargellini, P.: Sentinel-2: ESA's Optical High-Resolution Mission for GMES Operational Services, Remote Sensing of Environment, 120, 25–36, https://doi.org/10.1016/j.rse.2011.11.026, https://www.sciencedirect.com/science/article/pii/S0034425712000636, 2012.

Duchemin, B., Maisongrande, P., Boulet, G., and Benhadj, I.: A simple algorithm for yield estimates: Evaluation for semi-arid irrigated winter wheat monitored with green leaf area index, Environmental Modelling & Software, 23, 876–892, https://doi.org/10.1016/j.envsoft.2007.10.003, https://www.sciencedirect.com/science/article/pii/S1364815207002010, 2008.

Dumont, B., Leemans, V., Mansouri, M., Bodson, B., Destain, J. P., and Destain, M. F.: Parameter identification of the STICS crop model, using an accelerated formal MCMC approach, Environmental Modelling & Software, 52, 121–135, https://doi.org/10.1016/j.envsoft.2013.10.022, https://www.sciencedirect.com/science/article/pii/S136481521300265X, 2014.

Ellili, Y., Walter, C., Michot, D., Pichelin, P., and Lemercier, B.: Mapping soil organic carbon stock change by soil monitoring and digital soil mapping at the landscape scale, Geoderma, 351, 1–8, https://doi.org/10.1016/j.geoderma.2019.03.005, https://www.sciencedirect.com/science/article/pii/S0016706117320633, 2019.

Fieuzal, R., Marais Sicre, C., and Baup, F.: Estimation of Sunflower Yield Using a Simplified Agrometeorological Model Controlled by Optical and SAR Satellite Data, IEEE Journal of Selected Topics in Applied Earth Observations and Remote Sensing, 10, 5412–5422, https://doi.org/10.1109/JSTARS.2017.2737656, conference Name: IEEE Journal of Selected Topics in Applied Earth Observations and Remote Sensing, 2017.

Féret, J. B., Gitelson, A. A., Noble, S. D., and Jacquemoud, S.: PROSPECT-D: Towards modeling leaf optical properties through a complete lifecycle, Remote Sensing of Environment, 193, 204–215, https://doi.org/10.1016/j.rse.2017.03.004, https://www.sciencedirect.com/science/article/pii/S0034425717300962, 2017.

Garrigues, S., Olioso, A., Carrer, D., Decharme, B., Calvet, J.-C., Martin, E., Moulin, S., and Marloie, O.: Impact of climate, vegetation, soil and crop management variables on multi-year ISBA-A-gs simulations of evapotranspiration over a Mediterranean crop site, Geoscientific Model Development, 8, 3033–3053, https://doi.org/10.5194/gmd-8-3033-2015, https://gmd.copernicus.org/articles/8/3033/2015/, publisher: Copernicus GmbH, 2015.

Gervois, S., Ciais, P., de Noblet-Ducoudré, N., Brisson, N., Vuichard, N., and Viovy, N.: Carbon and water balance of European croplands throughout the 20th century, Global Biogeochemical Cycles, 22, https://doi.org/10.1029/2007GB003018, https://onlinelibrary.wiley.com/doi/abs/10.1029/2007GB003018, _eprint: https://onlinelibrary.wiley.com/doi/pdf/10.1029/2007GB003018, 2008.

Gielen, B., Acosta, M., Altimir, N., Buchmann, N., Cescatti, A., Ceschia, E., Fleck, S., Hörtnagl, L., Klumpp, K., Kolari, P., Lohila, A., Loustau, D., Marañon-Jimenez, S., Manise, T., Matteucci, G., Merbold, L., Metzger, C., Moureaux, C., Montagnani, L., Nilsson, M. B., Osborne, B., Papale, D., Pavelka, M., Saunders, M., Simioni, G., Soudani, K., Sonnentag, O., Tallec, T., Tuittila, E.-S., Peichl, M., Pokorny, R., Vincke, C., and Wohlfahrt, G.: Ancillary vegetation measurements at ICOS ecosystem stations, International Agrophysics, 32, 645–664, https://doi.org/10.1515/intag-2017-0048, http://archive.sciendo.com/INTAG/intag.2017.32.issue-4/intag-2017-0048/intag-2017-0048.pdf, 2018.

Gilhespy, S. L., Anthony, S., Cardenas, L., Chadwick, D., del Prado, A., Li, C., Misselbrook, T., Rees, R. M., Salas, W., Sanz-Cobena, A., Smith, P., Tilston, E. L., Topp, C. F. E., Vetter, S., and Yeluripati, J. B.: First 20 years of DNDC (DeNitrification DeComposition): Model evolution, Ecological Modelling, 292, 51–62, https://doi.org/10.1016/j.ecolmodel.2014.09.004, https://www.sciencedirect.com/science/article/pii/S0304380014004190, 2014.

Gregory, P. J., Johnson, S. N., Newton, A. C., and Ingram, J. S. I.: Integrating pests and pathogens into the climate change/food security debate, Journal of Experimental Botany, 60, 2827–2838, https://doi.org/10.1093/jxb/erp080, https://doi.org/10.1093/jxb/erp080, 2009.

Grieve, B. D., Duckett, T., Collison, M., Boyd, L., West, J., Yin, H., Arvin, F., and Pearson, S.: The challenges posed by global broadacre crops in delivering smart agri-robotic solutions: A fundamental rethink is required, Global Food Security, 23, 116–124, https://doi.org/10.1016/j.gfs.2019.04.011, https://www.sciencedirect.com/science/article/pii/S2211912419300100, 2019.

Guenet, B., Moyano, F. E., Peylin, P., Ciais, P., and Janssens, I. A.: Towards a representation of priming on soil carbon decomposition in the global land biosphere model ORCHIDEE (version 1.9.5.2), Geoscientific Model Development, 9, 841–855, https://doi.org/10.5194/gmd-9-841-2016, https://gmd.copernicus.org/articles/9/841/2016/gmd-9-841-2016.html, publisher: Copernicus GmbH, 2016.

Hagolle, O., Colin, J., Coustance, S., Kettig, P., d'Angelo, P., Auer, S., Doxani, G., and Desjardins, C.: Sentinel-2 surface reflectance products generated by CNES and DLR: methods, validation and applications, in: ISPRS Annals of the Photogrammetry, Remote Sensing and Spatial Information Sciences, pp. 9–15, Copernicus Publications, Nice, France, https://doi.org/10.5194/isprs-annals-V-1-2021-9-2021, https://elib.dlr.de/134558/, 2021.

Hao, S., Ryu, D., Western, A., Perry, E., Bogena, H., and Franssen, H. J. H.: Performance of a wheat yield prediction model and factors influencing the performance: A review and meta-analysis, Agricultural Systems, 194, 103 278, https://doi.org/10.1016/j.agsy.2021.103278, https://www.sciencedirect.com/science/article/pii/S0308521X21002316, 2021.

Hararuk, O., Xia, J., and Luo, Y.: Evaluation and improvement of a global land model against soil carbon data using a Bayesian Markov chain Monte Carlo method, Journal of Geophysical Research: Biogeosciences, 119, 403–417, https://doi.org/10.1002/2013JG002535, https://onlinelibrary.wiley.com/doi/abs/10.1002/2013JG002535, _eprint: https://onlinelibrary.wiley.com/doi/pdf/10.1002/2013JG002535, 2014.

Huang, J., Gómez-Dans, J. L., Huang, H., Ma, H., Wu, Q., Lewis, P. E., Liang, S., Chen, Z., Xue, J.-H., Wu, Y., Zhao, F., Wang, J., and Xie, X.: Assimilation of remote sensing into crop growth models: Current status and perspectives, Agricultural and Forest Meteorology, 276-277, 107 609, https://doi.org/10.1016/j.agrformet.2019.06.008, https://linkinghub.elsevier.com/retrieve/pii/S0168192319302175, 2019.

Jacquemoud, S. and Baret, F.: PROSPECT: A model of leaf optical properties spectra, Remote Sensing of Environment, 34, 75–91, https://doi.org/10.1016/0034-4257(90)90100-Z, https://www.sciencedirect.com/science/article/pii/003442579090100Z, 1990.

Jacquemoud, S., Verhoef, W., Baret, F., Bacour, C., Zarco-Tejada, P. J., Asner, G. P., François, C., and Ustin, S. L.: PROSPECT+SAIL models: A review of use for vegetation characterization, Remote Sensing of Environment, 113, S56–S66, https://doi.org/10.1016/j.rse.2008.01.026, https://www.sciencedirect.com/science/article/pii/S0034425709000765, 2009.

Karhu, K., Mattila, T., Bergström, I., and Regina, K.: Biochar addition to agricultural soil increased CH4 uptake and water holding capacity – Results from a short-term pilot field study, Agriculture, Ecosystems & Environment, 140, 309–313, https://doi.org/10.1016/j.agee.2010.12.005, https://www.sciencedirect.com/science/article/pii/S0167880910003208, 2011.

Kumar, S. V., Mocko, D. M., Wang, S., Peters-Lidard, C. D., and Borak, J.: Assimilation of Remotely Sensed Leaf Area Index into the Noah-MP Land Surface Model: Impacts on Water and Carbon Fluxes and States over the Continental United States, Journal of Hydrometeorology, 20, 1359–1377, https://doi.org/10.1175/JHM-D-18-0237.1, https://journals.ametsoc.org/view/journals/hydr/20/7/jhm-d-18-0237_1.xml, publisher: American Meteorological Society Section: Journal of Hydrometeorology, 2019.

Launay, C., Constantin, J., Chlebowski, F., Houot, S., Graux, A.-I., Klumpp, K., Martin, R., Mary, B., Pellerin, S., and Therond, O.: Estimating the carbon storage potential and greenhouse gas emissions of French arable cropland using high-resolution modeling, Global Change Biology, 27, 1645–1661, 2021.

Liu, S., Peng, D., Zhang, B., Chen, Z., Yu, L., Chen, J., Pan, Y., Zheng, S., Hu, J., Lou, Z., Chen, Y., and Yang, S.: The Accuracy of Winter Wheat Identification at Different Growth Stages Using Remote Sensing, Remote Sensing, 14, 893, https://doi.org/10.3390/rs14040893, https://www.mdpi.com/2072-4292/14/4/893, number: 4 Publisher: Multidisciplinary Digital Publishing Institute, 2022.

Lugato, E., Cescatti, A., Jones, A., Ceccherini, G., and Duveiller, G.: Maximising climate mitigation potential by carbon and radiative agricultural land management with cover crops, Environmental Research Letters, 15, 094 075, https://doi.org/10.1088/1748-9326/aba137, https://doi.org/10.1088/1748-9326/aba137, publisher: IOP Publishing, 2020.

Ma, R., Xiao, J., Liang, S., Ma, H., He, T., Guo, D., Liu, X., and Lu, H.: Pixel-level parameter optimization of a terrestrial biosphere model for improving estimation of carbon fluxes with an efficient model–data fusion method and satellite-derived LAI and GPP data, Geoscientific Model Development, 15, 6637–6657, https://doi.org/10.5194/gmd-15-6637-2022, https://gmd.copernicus.org/articles/15/6637/2022/, publisher: Copernicus GmbH, 2022.

Magnin, L.: La politique agricole commune et les données retardataires, Techniques & Culture. Revue semestrielle d'anthropologie des techniques, pp. 130–143, https://doi.org/10.4000/tc.12329, https://journals.openedition.org/tc/12329, iSBN: 9782713227875 Number: 72 Publisher: Les Éditions de l'EHESS, 2019.

Matthews, H. D., Zickfeld, K., Dickau, M., MacIsaac, A. J., Mathesius, S., Nzotungicimpaye, C.-M., and Luers, A.: Temporary nature-based carbon removal can lower peak warming in a well-below 2 °C scenario, Communications Earth & Environment, 3, 1–8, https://doi.org/10.1038/s43247-022-00391-z, https://www.nature.com/articles/s43247-022-00391-z, number: 1 Publisher: Nature Publishing Group, 2022.

Monteith, J. L., Moss, C. J., Cooke, G. W., Pirie, N. W., and Bell, G. D. H.: Climate and the efficiency of crop production in Britain, Philosophical Transactions of the Royal Society of London. B, Biological Sciences, 281, 277–294, https://doi.org/10.1098/rstb.1977.0140, https://royalsocietypublishing.org/doi/abs/10.1098/rstb.1977.0140, publisher: Royal Society, 1977.

Muñoz-Sabater, J., Dutra, E., Agustí-Panareda, A., Albergel, C., Arduini, G., Balsamo, G., Boussetta, S., Choulga, M., Harrigan, S., Hersbach, H., Martens, B., Miralles, D. G., Piles, M., Rodríguez-Fernández, N. J., Zsoter, E., Buontempo, C., and Thépaut, J.-N.: ERA5-Land: a state-of-the-art global reanalysis dataset for land applications, Earth System Science Data, 13, 4349–4383, https://doi.org/10.5194/essd-13-4349-2021, https://essd.copernicus.org/articles/13/4349/2021/, publisher: Copernicus GmbH, 2021.

Météo-France: Bilans climatiques annuels de 2014 à 2018 | Météo-FranceBilans climatiques annuels de 2014, 2015, 2016, 2017, 2018., https://meteofrance.fr/actualite/publications/les-publications-de-meteo-france/bilans-climatiques-annuels-de-2014-2018, 2019.

Météo-France: 2019 : les bilans climatiques | Météo-France 2019 : les bilans climatiques, https://meteofrance.fr/actualite/publications/les-publications-de-meteo-france/2019-les-bilans-climatiques, 2021.

Nevalainen, O., Niemitalo, O., Fer, I., Juntunen, A., Mattila, T., Koskela, O., Kukkamäki, J., Höckerstedt, L., Mäkelä, L., Jarva, P., Heimsch, L., Vekuri, H., Kulmala, L., Stam, A., Kuusela, O., Gerin, S., Viskari, T., Vira, J., Hyväluoma, J., Tuovinen, J.-P., Lohila, A., Laurila, T., Heinonsalo, J., Aalto, T., Kunttu, I., and Liski, J.: Towards agricultural soil carbon monitoring, reporting, and verification through the Field Observatory Network (FiON), Geoscientific Instrumentation, Methods and Data Systems, 11, 93–109, https://doi.org/10.5194/gi-11-93-2022, https://gi.copernicus.org/articles/11/93/2022/, publisher: Copernicus GmbH, 2022.

Nowak, B.: Precision Agriculture: Where do We Stand? A Review of the Adoption of Precision Agriculture Technologies on Field Crops Farms in Developed Countries, Agricultural Research, 10, 515–522, https://doi.org/10.1007/s40003-021-00539-x, https://doi.org/10.1007/s40003-021-00539-x, 2021.

Parker, W. S.: Ensemble modeling, uncertainty and robust predictions, WIREs Climate Change, 4, 213–223, https://doi.org/10.1002/wcc.220, https://onlinelibrary.wiley.com/doi/abs/10.1002/wcc.220, _eprint: https://onlinelibrary.wiley.com/doi/pdf/10.1002/wcc.220, 2013.

Parton, W. J., Hartman, M., Ojima, D., and Schimel, D.: DAYCENT and its land surface submodel: description and testing, Global and planetary Change, 19, 35–48, 1998.

Paustian, K., Larson, E., Kent, J., Marx, E., and Swan, A.: Soil C Sequestration as a Biological Negative Emission Strategy, Frontiers in Climate, 0, https://doi.org/10.3389/fclim.2019.00008, https://www.frontiersin.org/articles/10.3389/fclim.2019.00008/full, publisher: Frontiers, 2019.

Pique, G., Fieuzal, R., Al Bitar, A., Veloso, A., Tallec, T., Brut, A., Ferlicoq, M., Zawilski, B., Dejoux, J.-F., Gibrin, H., and Ceschia, E.: Estimation of daily CO2 fluxes and of the components of the carbon budget for winter wheat by the assimilation of Sentinel 2-like remote sensing data into a crop model, Geoderma, 376, 114 428, https://doi.org/10.1016/j.geoderma.2020.114428, https://linkinghub.elsevier.com/retrieve/pii/S0016706119321998, 2020a.

Pique, G., Fieuzal, R., Debaeke, P., Al Bitar, A., Tallec, T., and Ceschia, E.: Combining High-Resolution Remote Sensing Products with a Crop Model to Estimate Carbon and Water Budget Components: Application to Sunflower, Remote Sensing, 12, 2967, https://doi.org/10.3390/rs12182967, https://www.mdpi.com/2072-4292/12/18/2967, number: 18 Publisher: Multidisciplinary Digital Publishing Institute, 2020b.

Poeplau, C. and Don, A.: Carbon sequestration in agricultural soils via cultivation of cover crops – A meta-analysis, Agriculture, Ecosystems & Environment, 200, 33–41, https://doi.org/10.1016/j.agee.2014.10.024, https://www.sciencedirect.com/science/article/pii/S0167880914004873, 2015.

Porter, C. H., Jones, J. W., Adiku, S., Gijsman, A. J., Gargiulo, O., and Naab, J. B.: Modeling organic carbon and carbon-mediated soil processes in DSSAT v4.5, Operational Research, 10, 247–278, https://doi.org/10.1007/s12351-009-0059-1, https://doi.org/10.1007/s12351-009-0059-1, 2010.

Porter, J. R., Howden, M., and Smith, P.: Considering agriculture in IPCC assessments, Nature Climate Change, 7, 680–683, https://doi.org/10.1038/nclimate3404, https://www.nature.com/articles/nclimate3404, number: 10 Publisher: Nature Publishing Group, 2017.

Pörtner, H. O., Roberts, D. C., Adams, H., Adler, C., Aldunce, P., Ali, E., Begum, R. A., Betts, R., Kerr, R. B., Biesbroek, R., Birkmann, J., Bowen, K., Castellanos, E., Cissé, G., Constable, A., Cramer, W., Dodman, D., Eriksen, S. H., Fischlin, A., Garschagen, M., Glavovic, B., Gilmore, E., Haasnoot, M., Harper, S., Hasegawa, T., Hayward, B., Hirabayashi, Y., Howden, M., Kalaba, K., Kiessling, W., Lasco, R., Lawrence, J., Lemos, M. F., Lempert, R., Ley, D., Lissner, T., Lluch-Cota, S., Loeschke, S., Lucatello, S., Luo, Y., Mackey, B., Maharaj, S., Mendez, C., Mintenbeck, K., Vale, M. M., Morecroft, M. D., Mukherji, A., Mycoo, M., Mustonen, T., Nalau, J., Okem, A., Ometto, J. P., Parmesan, C., Pelling, M., Pinho, P., Poloczanska, E., Racault, M.-F., Reckien, D., Pereira, J., Revi, A., Rose, S., Sanchez-Rodriguez, R., Schipper, E. L. F., Schmidt, D., Schoeman, D., Shaw, R., Singh, C., Solecki, W., Stringer, L., Thomas, A., Totin, E., Trisos, C., Viner, D., Aalst, M. v., Wairiu, M., Warren, R., Yanda, P., and Ibrahim, Z. Z.: Climate change 2022: impacts, adaptation and vulnerability, https://research.wur.nl/en/publications/climate-change-2022-impacts-adaptation-and-vulnerability, publisher: IPCC, 2022.

Reichstein, M., Falge, E., Baldocchi, D., Papale, D., Aubinet, M., Berbigier, P., Bernhofer, C., Buchmann, N., Gilmanov, T., Granier, A., Grünwald, T., Havránková, K., Ilvesniemi, H., Janous, D., Knohl, A., Laurila, T., Lohila, A., Loustau, D., Matteucci, G., Meyers, T., Miglietta, F., Ourcival, J.-M., Pumpanen, J., Rambal, S., Rotenberg, E., Sanz, M., Tenhunen, J., Seufert, G., Vaccari, F., Vesala, T., Yakir, D., and Valentini, R.: On the separation of net ecosystem exchange into assimilation and ecosystem respiration: review and improved algorithm, Global Change Biology, 11, 1424–1439, https://doi.org/10.1111/j.1365-2486.2005.001002.x, http://onlinelibrary.wiley.com/doi/abs/10.1111/j.1365-2486.2005.001002.x, _eprint: https://onlinelibrary.wiley.com/doi/pdf/10.1111/j.1365-2486.2005.001002.x, 2005.

Roderick, M. L., Farquhar, G. D., Berry, S. L., and Noble, I. R.: On the direct effect of clouds and atmospheric particles on the productivity and structure of vegetation, Oecologia, 129, 21–30, https://doi.org/10.1007/s004420100760, https://doi.org/10.1007/s004420100760, 2001.

Roy, D. P., Wulder, M. A., Loveland, T. R., C.e., W., Allen, R. G., Anderson, M. C., Helder, D., Irons, J. R., Johnson, D. M., Kennedy, R., Scambos, T. A., Schaaf, C. B., Schott, J. R., Sheng, Y., Vermote, E. F., Belward, A. S., Bindschadler, R., Cohen, W. B., Gao, F., Hipple, J. D., Hostert, P., Huntington, J., Justice, C. O., Kilic, A., Kovalskyy, V., Lee, Z. P., Lymburner, L., Masek, J. G., McCorkel, J., Shuai, Y., Trezza, R., Vogelmann, J., Wynne, R. H., and Zhu, Z.: Landsat-8: Science and product vision for terrestrial global change research, Remote Sensing of Environment, 145, 154–172, https://doi.org/10.1016/j.rse.2014.02.001, https://www.sciencedirect.com/science/article/pii/S003442571400042X, 2014.

Seidel, S. J., Palosuo, T., Thorburn, P., and Wallach, D.: Towards improved calibration of crop models – Where are we now and where should we go?, European Journal of Agronomy, 94, 25–35, https://doi.org/10.1016/j.eja.2018.01.006, https://www.sciencedirect.com/science/article/pii/S1161030118300066, 2018.

Sharma, A., Jain, A., Gupta, P., and Chowdary, V.: Machine Learning Applications for Precision Agriculture: A Comprehensive Review, IEEE Access, 9, 4843–4873, https://doi.org/10.1109/ACCESS.2020.3048415, conference Name: IEEE Access, 2021.

SIE: SIE - System d'Information Environementale, https://sie.cesbio.omp.eu/variables.php, 2022.

Skakun, S., Wevers, J., Brockmann, C., Doxani, G., Aleksandrov, M., Batič, M., Frantz, D., Gascon, F., Gómez-Chova, L., Hagolle, O., López-Puigdollers, D., Louis, J., Lubej, M., Mateo-García, G., Osman, J., Peressutti, D., Pflug, B., Puc, J., Richter, R., Roger, J.-C., Scaramuzza, P., Vermote, E., Vesel, N., Zupanc, A., and Žust, L.: Cloud Mask Intercomparison eXercise (CMIX): An evaluation of cloud masking algorithms for Landsat 8 and Sentinel-2, Remote Sensing of Environment, 274, 112 990, https://doi.org/10.1016/j.rse.2022.112990, https://www.sciencedirect.com/science/article/pii/S0034425722001043, 2022.

Skea, J., Shukla, P., and Kılkıs, S.: Climate Change 2022: Mitigation of Climate Change, Tech. rep., Cambridge University Press, Cambridge (MA), USA, https://open.metu.edu.tr/handle/11511/97072, 2022.

Smith, P., Lanigan, G., Kutsch, W. L., Buchmann, N., Eugster, W., Aubinet, M., Ceschia, E., Béziat, P., Yeluripati, J. B., Osborne, B., Moors, E. J., Brut, A., Wattenbach, M., Saunders, M., and Jones, M.: Measurements necessary for assessing the net ecosystem carbon budget of croplands, Agriculture, Ecosystems & Environment, 139, 302–315, https://doi.org/10.1016/j.agee.2010.04.004, https://linkinghub.elsevier.com/retrieve/pii/S016788091000112X, 2010.

Smith, P., Soussana, J.-F., Angers, D., Schipper, L., Chenu, C., Rasse, D. P., Batjes, N. H., van Egmond, F., McNeill, S., Kuhnert, M., Arias-Navarro, C., Olesen, J. E., Chirinda, N., Fornara, D., Wollenberg, E., Álvaro Fuentes, J., Sanz-Cobena, A., and Klumpp, K.: How to measure, report and verify soil carbon change to realize the potential of soil carbon sequestration for atmospheric greenhouse gas removal, Global Change Biology, 26, 219–241, https://doi.org/10.1111/gcb.14815, https://onlinelibrary.wiley.com/doi/abs/10.1111/gcb.14815, _eprint: https://onlinelibrary.wiley.com/doi/pdf/10.1111/gcb.14815, 2020.

Song, X.-P., Huang, W., Hansen, M. C., and Potapov, P.: An evaluation of Landsat, Sentinel-2, Sentinel-1 and MODIS data for crop type mapping, Science of Remote Sensing, 3, 100 018, https://doi.org/10.1016/j.srs.2021.100018, https://www.sciencedirect.com/science/article/pii/S2666017221000055, 2021.

Soriano-González, J., Angelats, E., Martínez-Eixarch, M., and Alcaraz, C.: Monitoring rice crop and yield estimation with Sentinel-2 data, Field Crops Research, 281, 108 507, https://doi.org/10.1016/j.fcr.2022.108507, https://www.sciencedirect.com/science/article/pii/S0378429022000788, 2022.

Soussana, J.-F., Lutfalla, S., Ehrhardt, F., Rosenstock, T., Lamanna, C., Havlík, P., Richards, M., Wollenberg, E. L., Chotte, J.-L., Torquebiau, E., Ciais, P., Smith, P., and Lal, R.: Matching policy and science: Rationale for the '4 per 1000 - soils for food security and climate' initiative, Soil and Tillage Research, 188, 3–15, https://doi.org/10.1016/j.still.2017.12.002, https://www.sciencedirect.com/science/article/pii/S0167198717302271, 2019.

Steinbeiss, S., Gleixner, G., and Antonietti, M.: Effect of biochar amendment on soil carbon balance and soil microbial activity, Soil Biology and Biochemistry, 41, 1301–1310, https://doi.org/10.1016/j.soilbio.2009.03.016, https://www.sciencedirect.com/science/article/pii/S0038071709001242, 2009.

Stevens, A., van Wesemael, B., Bartholomeus, H., Rosillon, D., Tychon, B., and Ben-Dor, E.: Laboratory, field and airborne spectroscopy for monitoring organic carbon content in agricultural soils, Geoderma, 144, 395–404, https://doi.org/10.1016/j.geoderma.2007.12.009, https://www.sciencedirect.com/science/article/pii/S001670610700362X, 2008.

Su, Y.-Z., Wang, F., Suo, D.-R., Zhang, Z.-H., and Du, M.-W.: Long-term effect of fertilizer and manure application on soil-carbon sequestration and soil fertility under the wheat–wheat–maize cropping system in northwest China, Nutrient Cycling in Agroecosystems, 75, 285–295, https://doi.org/10.1007/s10705-006-9034-x, https://doi.org/10.1007/s10705-006-9034-x, 2006.

Suits, G. H.: The calculation of the directional reflectance of a vegetative canopy, Remote Sensing of Environment, 2, 117–125, https://doi.org/10.1016/0034-4257(71)90085-X, https://www.sciencedirect.com/science/article/pii/003442577190085X, 1971.

Supit, I., Hoojer, A., and Diepen, C.: System description of the Wofost 6.0 crop simulation model implemented in CGMS. Volume 1: Theory and Algorithms, 1994.

Tewes, A., Hoffmann, H., Krauss, G., Schäfer, F., Kerkhoff, C., and Gaiser, T.: New Approaches for the Assimilation of LAI Measurements into a Crop Model Ensemble to Improve Wheat Biomass Estimations, Agronomy, 10, 446, https://doi.org/10.3390/agronomy10030446, https://www.mdpi.com/2073-4395/10/3/446, number: 3 Publisher: Multidisciplinary Digital Publishing Institute, 2020.

Trepos, R., Champolivier, L., Dejoux, J.-F., Al Bitar, A., Casadebaig, P., and Debaeke, P.: Forecasting Sunflower Grain Yield by Assimilating Leaf Area Index into a Crop Model, Remote Sensing, 12, 3816, https://doi.org/10.3390/rs12223816, https://hal.inrae.fr/hal-03108921, 2020.

Upreti, D., Pignatti, S., Pascucci, S., Tolomio, M., Huang, W., and Casa, R.: Bayesian Calibration of the Aquacrop-OS Model for Durum Wheat by Assimilation of Canopy Cover Retrieved from VENμS Satellite Data, Remote Sensing, 12, 2666, https://doi.org/10.3390/rs12162666, https://www.mdpi.com/2072-4292/12/16/2666, number: 16 Publisher: Multidisciplinary Digital Publishing Institute, 2020.

Vaudour, E., Gomez, C., Loiseau, T., Baghdadi, N., Loubet, B., Arrouays, D., Ali, L., and Lagacherie, P.: The Impact of Acquisition Date on the Prediction Performance of Topsoil Organic Carbon from Sentinel-2 for Croplands, Remote Sensing, 11, 2143, https://doi.org/10.3390/rs11182143, https://www.mdpi.com/2072-4292/11/18/2143, number: 18 Publisher: Multidisciplinary Digital Publishing Institute, 2019.

Veloso, A., Mermoz, S., Bouvet, A., Le Toan, T., Planells, M., Dejoux, J.-F., and Ceschia, E.: Understanding the temporal behavior of crops using Sentinel-1 and Sentinel-2-like data for agricultural applications, Remote Sensing of Environment, 199, 415–426, https://doi.org/10.1016/j.rse.2017.07.015, https://www.sciencedirect.com/science/article/pii/S0034425717303309, 2017.

Veloso, A. G. M.: Modélisation spatialisée de la production, des flux et des bilans de carbone et d'eau des cultures de blé à l'aide de données de télédétection : application au sud-ouest de la France, These de doctorat, Toulouse 3, http://www.theses.fr/2014TOU30092, 2014.

Verhoef, W.: Light scattering by leaf layers with application to canopy reflectance modeling: The SAIL model, Remote Sensing of Environment, 16, 125–141, https://doi.org/10.1016/0034-4257(84)90057-9, https://www.sciencedirect.com/science/article/pii/0034425784900579, 1984.

Verhoef, W., Jia, L., Xiao, Q., and Su, Z.: Unified Optical-Thermal Four-Stream Radiative Transfer Theory for Homogeneous Vegetation Canopies, IEEE Transactions on Geoscience and Remote Sensing, 45, 1808–1822, https://doi.org/10.1109/TGRS.2007.895844, conference Name: IEEE Transactions on Geoscience and Remote Sensing, 2007.

Vidal, J.-P., Martin, E., Franchistéguy, L., Baillon, M., and Soubeyroux, J.-M.: A 50-year high-resolution atmospheric reanalysis over France with the Safran system, International Journal of Climatology, 30, 1627–1644, https://doi.org/10.1002/joc.2003, https://onlinelibrary.wiley.com/doi/abs/10.1002/joc.2003, _eprint: https://onlinelibrary.wiley.com/doi/pdf/10.1002/joc.2003, 2010.

Vrugt, J. A.: Markov chain Monte Carlo simulation using the DREAM software package: Theory, concepts, and MATLAB implementation, Environmental Modelling & Software, 75, 273–316, https://doi.org/10.1016/j.envsoft.2015.08.013, https://www.sciencedirect.com/science/article/pii/S1364815215300396, 2016.

Wall, D. H., Nielsen, U. N., and Six, J.: Soil biodiversity and human health, Nature, 528, 69–76, https://doi.org/10.1038/nature15744, https://www.nature.com/articles/nature15744, number: 7580 Publisher: Nature Publishing Group, 2015.

Wang, J., Lopez-Lozano, R., Weiss, M., Buis, S., Li, W., Liu, S., Baret, F., and Zhang, J.: Crop specific inversion of PROSAIL to retrieve green area index (GAI) from several decametric satellites using a Bayesian framework, Remote Sensing of Environment, 278, 113 085, https://doi.org/10.1016/j.rse.2022.113085, https://www.sciencedirect.com/science/article/pii/S0034425722001997, 2022.

Wattenbach, M., Sus, O., Vuichard, N., Lehuger, S., Gottschalk, P., Li, L., Leip, A., Williams, M., Tomelleri, E., Kutsch, W. L., Buchmann, N., Eugster, W., Dietiker, D., Aubinet, M., Ceschia, E., Béziat, P., Grünwald, T., Hastings, A., Osborne, B., Ciais, P., Cellier, P., and Smith, P.: The carbon balance of European croplands: A cross-site comparison of simulation models, Agriculture, Ecosystems & Environment, 139, 419–453, https://doi.org/10.1016/j.agee.2010.08.004, https://www.sciencedirect.com/science/article/pii/S0167880910002070, 2010.

Weiss, M., Jacob, F., and Duveiller, G.: Remote sensing for agricultural applications: A meta-review, Remote Sensing of Environment, 236, 111 402, https://doi.org/10.1016/j.rse.2019.111402, https://www.sciencedirect.com/science/article/pii/S0034425719304213, 2020.

Woodwell, G. M. and Whittaker, R. H.: Primary Production in Terrestrial Ecosystems, American Zoologist, 8, 19–30, https://doi.org/10.1093/icb/8.1.19, https://academic.oup.com/icb/article-lookup/doi/10.1093/icb/8.1.19, 1968.

Zhang, Q., Xiao, X., Braswell, B., Linder, E., Baret, F., and Moore, B.: Estimating light absorption by chlorophyll, leaf and canopy in a deciduous broadleaf forest using MODIS data and a radiative transfer model, Remote Sensing of Environment, 99, 357–371, https://doi.org/10.1016/j.rse.2005.09.009, https://www.sciencedirect.com/science/article/pii/S0034425705003044, 2005.

Zhuo, W., Huang, J., Xiao, X., Huang, H., Bajgain, R., Wu, X., Gao, X., Wang, J., Li, X., and Wagle, P.: Assimilating remote sensing-based VPM GPP into the WOFOST model for improving regional winter wheat yield estimation, European Journal of Agronomy, 139, 126 556, https://doi.org/10.1016/j.eja.2022.126556, https://www.sciencedirect.com/science/article/pii/S1161030122001046, 2022.